frontiers in Earth Science

TYPE Original Research
PUBLISHED 28 April 2026
DOI 10.3389/feart.2026.1759842

Check for updates

OPEN ACCESS

EDITED BY
Dicky Harishidayat,
Pertamina Hulu Energi, Indonesia

REVIEWED BY
Cristina Roque,
Estrutura de Missão para a Extensão da Plataforma Continental, Portugal
Michael Steventon,
Shell, United Kingdom
Fermin Palma,
National Scientific and Technical Research Council (CONICET), Argentina
Paul Morris,
BP, United Kingdom

*CORRESPONDENCE
Lealern Beza Zerihun,
zerihun@geol.rwth-aachen.de

RECEIVED 03 December 2025
REVISED 18 January 2026
ACCEPTED 23 March 2026
PUBLISHED 28 April 2026

CITATION
Zerihun LB, Parlevliet A, Adema P, Eggenhuisen JT, Winsemann J and Spychala YT (2026) Self-organization of turbiditic lobe deposits: insights on stacking patterns and flow field evolution from analogue experiments under constant boundary conditions. *Front. Earth Sci.* 14:1759842. doi: 10.3389/feart.2026.1759842

COPYRIGHT
© 2026 Zerihun, Parlevliet, Adema, Eggenhuisen, Winsemann and Spychala. This is an open-access article distributed under the terms of the Creative Commons Attribution License (CC BY). The use, distribution or reproduction in other forums is permitted, provided the original author(s) and the copyright owner(s) are credited and that the original publication in this journal is cited, in accordance with accepted academic practice. No use, distribution or reproduction is permitted which does not comply with these terms.

Self-organization of turbiditic lobe deposits: insights on stacking patterns and flow field evolution from analogue experiments under constant boundary conditions

Lealern Beza Zerihun[1]*, Aniela Parlevliet[2], Pelle Adema[2], Joris T. Eggenhuisen[2], Jutta Winsemann[3] and Yvonne T. Spychala[1]

[1]Chair of Geology and Sedimentary Systems and Geological Institute, RWTH Aachen University, Aachen, Germany, [2]Department of Earth Sciences, Utrecht University, Utrecht, Netherlands, [3]Institute of Earth System Sciences, Leibniz University Hannover, Hannover, Germany

Depositional patterns of submarine lobes are driven by a combination of allogenic (e.g., climate, tectonics) and autogenic processes (e.g., avulsion, bifurcation). However, the impact of autogenic processes and their influence on the formation and evolution of submarine lobes remain poorly understood. Studying these internal dynamics in the outcrop or in the deep sea is challenging due to natural deposits recording a mixture of autogenic and allogenic signals. To examine the autogenic development of submarine lobes, three series of experiments were conducted under constant boundary conditions in the Eurotank Flume Laboratory. Emphasis was placed on documenting stacking patterns and the evolution of turbidity currents relative to topography. The resulting deposits display three stacking patterns: compensational, aggradational, and retrogradational. The velocity of the turbidity currents (measured in the basin floor beyond the break-of-slope) decreased with each subsequent run, along with the development of backstepping, lateral spreading and thinning upward trend in the basin floor deposits. These depositional patterns are interpreted as a result of successively increasing sediment retention in the channel. These results suggest that autogenic processes in sand-rich turbidite systems create complex sediment stacking patterns, ranging from aggradation to retrogradation. Progradational stacking patterns were not observed in any of the experimental series, which suggests that progradation is likely controlled by allogenic processes. This experimental study, addressing characteristics of autogenically formed lobe deposits, will help with disentanglement of the autogenic "noise" from the external signal record stored in the deposits and enable better assessment of climate and tectonic signals.

KEYWORDS
analogue modelling, autogenic processes, flow field evolution, stacking patterns, turbidity currents

1 Introduction

Submarine fans are among the largest sedimentary systems on Earth. They are deposited by gravity flows at the base of continental slopes or in intraslope basins and formed by the deposition of lobes. The spatial arrangement and morphological development of lobes respond to a combination of external (allogenic) and internal (autogenic) processes. These processes control sediment supply and transport pathways, and thus the depositional record used to reconstruct paleoenvironmental conditions in Earth's history (Normark et al., 2006; Romans et al., 2016).

Allogenic controls (eustatic sea-level variations, climatic fluctuations, and tectonic activity) influence sediment supply and transport, which shape global and local depositional patterns (Posamentier and Kolla, 2003; Knudson and Hendy, 2009). Autogenic processes, particularly those responsible for the evolution of submarine lobes and their feeder channels, include avulsion, levee growth, and compensational stacking, which disrupt sediment dispersal pathways and can lead to rapid changes in depocenters (e.g., Straub and Pyles, 2012; Deptuck and Sylvester, 2018). The interplay of these autogenic processes results in the dynamic organization of channel-lobe systems, sediment routing, and depositional patterns in submarine fan system (Morris et al., 2024), which influence the stratigraphic architecture and heterogeneity of deep-marine deposits.

Grime et al. (2024) investigated the autogenic and allogenic controls on turbidite lobe stacking in the Dønna Terrace system and highlighted the stacking patterns arise from the interplay between autogenic compensational lobe-migration processes and allogenic variations in sediment supply. However, it is difficult to fully understand and accurately assign data to geomodels regarding the influence of autogenic processes on submarine fan systems from outcrops and core datasets because of limited access, incomplete depositional records and overprinting of autogenic and allogenic signals in natural deposits.

Beerbower (1964) previously suggested that there are various ways in which allogenic and autogenic processes interrelate with each other. Their interaction results in four possible outcomes: the allogenic signal can be 1) reduced, 2) amplified, 3) overprinted, or 4) removed by autogenic processes. A combination of outcome 1, 3, and 4 leads to the more recent notion that allogenic signals are often "*shredded*" (Jerolmack and Paola, 2010). This hypothesis raises questions about the faithfulness of environmental signal preservation in deposits (Blum et al., 2018; Romans et al., 2016).

Several physical experiments, addressing the formation of turbidite systems under specific allogenic and/or autogenic conditions have been performed in the last decade (Hamilton et al., 2015; Fick et al., 2017; Ferguson et al., 2020; Spychala et al., 2020). Ferguson et al. (2020) explored how autogenic and allogenic controls influence the development of submarine fans. Their work demonstrated that while external signals can be preserved, they are obscured by autogenic processes over time. Fick et al. (2017) investigated autogenic controls on submarine fan topography and geometry, revealing significant morphological variability under steady-state flow conditions. Similarly, Hamilton et al. (2015) also conducted experiments focused on autogenic avulsion processes and demonstrated that mouth-bar aggradation and hydraulic jumps are the main factors driving channel reorganization and flow redirection. This previous research has provided many insights into individual depositional events and morphodynamic feedbacks. But, none of those experimental studies addressed how autogenic processes shape the sedimentary architecture or stacking patterns of channel-lobe systems through time.

In addition to physical experiments and outcrop studies, computer models such as Lobyte3D were used to simulate the evolution of submarine fans, capturing both autogenic and allogenic processes (Pyrcz et al., 2005; Burgess and Duller, 2019; Burgess and Duller, 2024). This body of work provides compelling evidence that self-organized depositional architectures can develop characteristic geometries and stacking patterns without external constraints, highlighting the importance of autogenic controls on submarine fan formation.

However, despite these advances, a fundamental limitation remains in our ability to understand the effects of purely autogenic processes on trends in stratal stacking patterns, channel sediment retention, and sediment distribution within the submarine fan system. This study tackles this problem by examining how autogenic signals influence the depositional patterns of channels and lobes over successive flow events. In doing so, it offers a framework for researchers to better tell apart autogenic variability from allogenic signals, thereby improving the accuracy of reconstruction of the influence of sediment supply cycle variations on deep-water architecture.

The questions that arise here are: what stratal stacking patterns can be documented from submarine fans formed solely by autogenic processes? How are sediments distributed between the channel and the submarine lobe under constant boundary conditions? Do autogenic processes have a significant impact on flow evolution and depositional architecture of channels and lobe systems?

To address these knowledge gaps, three series of experiments under constant boundary condition were conducted at Utrecht University in the Eurotank Flume Laboratory. The specific aims of this study are: (1) to document stacking patterns, sediment dispersal patterns, and the channel and lobe morphology that arise under constant boundary conditions; (2) to investigate the evolution of the flow field of turbidity currents over a topographically changing lobe; and (3) to better understand the role of autogenic processes in controlling the morphology, sediment distribution, and architecture of submarine lobes.

2 Materials and methods

2.1 Set-up and procedure

The Eurotank measures 11 m × 6 m × 1.2 m. The flume configuration featured a slope and channel (Table 1) with a gradient of 11°, which decreased to a gentler slope of 4° for the proximal basin floor and 0° for the distal basin floor (Figure 1). For all series, the channel length was 2.5 m. Experimental setups for channel dimensions and proximal basin floor length can be found in Table 1. The experimental setup builds upon flume setups by De Leeuw et al. (2018) and Spychala et al. (2020). Before each experiment, the flume was filled with water to a depth of 1.2 m 900 L of water-sediment mixture was prepared in a mixing tank and

TABLE 1 Eurotank experimental setup and parameters for Series 1, 2, and 3.

Parameter	Series 1	Series 2	Series 3
Proximal basin length (m)	3.1	2.9	2.6
Channel dimensions (cm)	80 × 8	70 × 8	70 × 8

introduced into the basin. The total duration of each experiment was around 100 s. The upper part of the inclined channel, close to the inlet, was reset once during Series 3 due to a built up of sediment right behind the inlet to maintain flow efficiency between successive experimental runs.

Each series represents a different configuration of sediment concentration and sediment mixture composition, which is kept constant during the individual runs conducted during these series (Table 2). The industrial grade materials used in this study included quartz sand (mineral density: 2,650 kg/m^3), ground glass silt (mineral density: 2,300 kg/m^3), silicon carbide (mineral density: 3,200 kg/m^3), garnet (mineral density: 3,900 kg/m^3), and corundum (mineral density: 4,000 kg/m^3). The grain sizes of the sediments used in series 1 and 2 were D_{50} = 148 µm, D_{10} = 35 µm, and D_{90} = 253 µm, while D_{50} = 146 µm, D_{10} = 32 µm, and D_{90} = 254 µm for series 3.

2.2 Scaling

The Shields parameter is a dimensionless quantity relevant to research on sediment transport in rivers and shallow seas (Shields, 1936), as well as experimental studies of turbidity currents (e.g., De Leeuw et al., 2016; Fernandes et al., 2020; Pohl et al., 2020). This present work utilized the Shields scale according to methodologies established by De Leeuw et al. (2016) and Pohl et al. (2020) to examine sediment deposition mechanics associated with turbulent flow interfaces and suspended sediment interactions. To ensure Shield Scaling in the setup, basin configuration (slope angle of 11° and basin angle of 4°) as well as sediment volume concentration need to be exaggerated compared to natural systems (slope of 1°–5°; Covault et al., 2007; Covault et al., 2011; Paull et al., 2018) to ensure sustained, fully turbulent, erosive flows at the laboratory scale, following published papers (e.g., De Leeuw et al., 2016; Pohl et al., 2020).

The Shields parameter (θ, Equation 1) and the particle Reynolds number (Re_p) Shields (1936) are calculated as follow:

$$\theta = \frac{\rho_t u_*^2}{(\rho_s - \rho_w) g d_t} \tag{1}$$

Where ρ_t is the density of the turbidity current, ρ_s the density of the suspended sediment (2,650 kg/m^3), ρ_w the density of the fluid (1,000 kg/m^3), d_t the grain size of the suspended sediment (D_{50}), and g the gravitational acceleration (9.81 m/s^2).

The density of the turbidity current calculated as (Equation 2):

$$\rho_t = (\rho_s - \rho_w) C + \rho_w \tag{2}$$

Where C is the sediment concentration used in the turbidity current experiments

The particle Reynolds number is determined by Equation 3:

$$Re_p = \frac{u_* d_b}{V} \tag{3}$$

Where $u*$ is the shear velocity, d_b is the grain size of the sediment of the bed = the grain size of the suspended sediment D_{50}, V is the kinematic viscosity (1^*10^{-6} m^2/s at 20 °C).

Shear velocity ($u*$) is calculated using the methods of Cartigny et al. (2014), Middleton and Southard (1984) and Van Rijn et al. (1993) (Equation 4):

$$u_* = \frac{U_{max} k}{\ln\left(\frac{h_{max}}{0.1 d_n}\right)} \tag{4}$$

Where U_{max} is the maximum time-averaged velocity, h_{max} is the height of the velocity maximum, k is the von Kármán's constant (0.40), and the $d_n = D_{90}$ of the grain size.

Flow characteristics can relate both field and laboratory data using the Shields parameter and the particle Reynolds number. In this research, suspended sediment concentrations reached very high levels of 17% and 19 vol%, corresponding to Shields parameter values (θ = 0.357–1.49) (Supplementary Figure S1; Supplementary Table S1). This range falls within the high-density turbidity currents regime (Kuenen and Migliorini, 1950; Cartigny et al., 2014). The particle Reynolds number in sloped channels spans values typical of transitionally rough conditions (Re_p ranging from 5 to 70) to those characteristics of hydraulically smooth conditions on basin floors (less than 5) (Garcia, 2008). In this context, fine-grained sand (D_{50} = 148 µm for series 1 and 2, and D_{50} = 146 µm for series 3) exhibits varying flow conditions throughout the cross-sectional tests. The flow conditions of all runs in series 1 and 2, as well as run 1 of series 3, were classified as transitionally rough conditions. Runs 2 of series 3 lies at the boundary between transitionally rough flow and hydraulically smooth flow, while Runs 3 and 4 are clearly within the hydraulically smooth range (Supplementary Figure S1). Further calculations of the Froude number (Fr, Equation 5) lead to insights regarding the flow regime of turbidity currents.

$$Fr = \frac{U}{\sqrt{g^* h}} \tag{5}$$

In all three series (1–3), the Froude number remains above 1 (Supplementary Table S1), except for Run 4 of series 3 (which is transitional to subcritical), indicating that the turbidity current can be interpreted as supercritical.

2.3 Velocity measurements

3D Ultrasonic Doppler Velocimetry (UDV) probes were used to measure the velocity of the turbidity current. The probes were positioned 1.75 m downstream of the break of slope (Figure 1) and mounted on a robotically moved gantry. This location was selected as it permits the full development of the turbidity current, allowing for velocity measurement before the current becomes less turbulent. The height of the probes was set at 18 cm from the bed and was adjusted based on the sediment deposited between runs. Measurements were conducted at seven lateral positions in the basin floor, ranging from 1.2 m to −1.2 m (left to right). However, the initial measuring

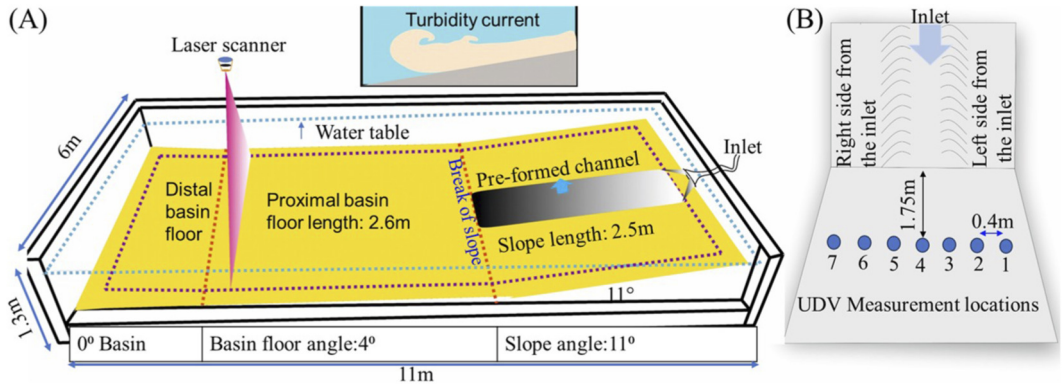


FIGURE 1
(A) A simple 3D flume tank setup of the Eurotank flume laboratory, featuring a channel angle of 11°and a proximal basin bottom angle of 4°. The water-sediment mixture was prepared in the mixing tank before being pumped through the inlet box and onto the slope at a constant discharge rate of 30 m^3/h. The flow was then directed into a defined channel at the bottom of the basin. **(B)** The location of the UDV and the basin orientation from the inlet. Flow velocities were measured using 3D ultrasonic Doppler velocimetry (UDV) at 40 cm intervals, starting 1.75 m downstream from the break in slope (BoS), with the blue dots indicating the measurement locations. Laser scanner data were utilized to generate digital elevation models (DEMs).

TABLE 2 **Sediment composition and concentration for Series 1, 2, and 3.**

Parameter	Series 1	Series 2	Series 3
Sand (%)	69.4	69.4	72
Silt (%)	23.1	23.1	25
Heavy minerals (%)	7.5	7.5	3
Sediment concentration (% vol)	17	17	19

point did not capture any velocity data, and only the velocity data from six measuring points are interpreted in the text. The positions were: 1.2 m, 0.8 m, 0.4 m, 0 m (centerline), −0.4 m, −0.8 m, and −1.2 m. To ensure accurate measurements at these locations, the UDV probes were aligned parallel to the basin floor at a 4° angle, matching its inclination. The measured velocity data is used to determine the time-averaged velocity of the turbidity current in the longitudinal, lateral and vertical turbulent flow, as well as to provide characterization of the flow dynamics in the basin.

2.4 Digital elevation models

A high-resolution 2 × 2 mm laser scanner was used to capture basin topography before and after each run (Figure 1). The data obtained from the laser scan are used to create digital elevation models (DEMs) to assess the effects of sedimentation and erosion on basin topography and the resulting stacking patterns of the deposits.

To assess sediment volume distribution in the channel and basin floor deposits during the three series of experiments, digital elevation data were collected before and after each run. Changes in sediment thickness were determined by subtracting the pre-run data from the post-run data. Using digital elevation data (DEM), sediment volumes were calculated to determine the total sediment volume for each run. Sediment volumes within the channel and on the basin floor were then expressed as percentages of the total sediment volume used in each run. This allowed for the estimation of the sediment volume in the channel-lobe system.

2.5 Study assumptions and limitations

Although the study provides insights into the autogenic development of submarine lobes it also has limitations and assumptions that need to be taken into account. Firstly hierarchy: This study assumes that deposits formed by a single turbidity current is representative of lobe element. These, in turn, stack over multiple runs to form a composite lobe (sensu Spychala et al., 2020; Ferguson et al., 2020). Although this hierarchy aids in experimental assessment, natural systems might be more complex and have layers of internal architectures that are not covered here.

Secondly, the experimental setup focused specifically on sand-prone systems using fine-grained sand. The study did not account for silt-prone mixtures, which, in all likelihood, would affect flow competence and deposition patterns, as these would be a function of varying settling velocities, grain interactions and flow field evolution They also represent only a subset of possible basin configurations, that would also influence depositional patterns (Spychala et al., 2020).

Thirdly, to achieve Shields scaling in a rough transitional regime, basin angles and sediment concentrations are exaggerated. Sediment concentration in natural systems are generally much lower averaged over the flow height (0.2–2.5%Vol; Pirmez and Imran, 2003; Konsoer et al., 2013). However, it is thought that the flow core of natural turbidity currents could be just as concentrated as the flows produced in our experiments (Peakall and Sumner, 2015).

Finally, almost all flows except Run 4 of Series 3 fall into the supercritical regime (see Supplementary Table S1) at the point of measurement 1.75 m behind the base of slope. This indicates that for the carried out experiments no hydraulic jump occurred in the region of the break of slope or channel-lobe-transition zone. However, Run 4 of Series 3 that shows itself to be transcritical

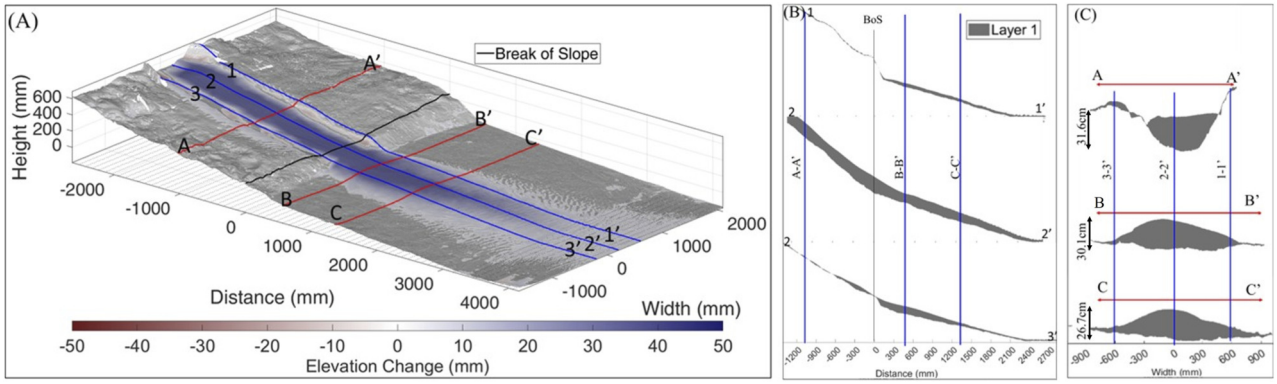


FIGURE 2
Maps of deposition and erosion in channel and lobe cross-sections of series 1. **(A)** Digital elevation map, **(B)** dip-section cumulative deposition, and **(C)** cross-sections with a vertical exaggeration of ×5.

indicates that with decreasing flow velocity the flows eventually experienced a change from super-to subcritical and the distal part of our deposits are formed by subcritical flows. If flows are essentially subcritical once they exit the channel is a common assumption and up to debate. Other experiments like Pohl et al. (2020) and datasets collected from natural systems, especially in small sand-rich fans question this assumption and suggest that proximal parts of lobe deposits could be formed by supercritical flows (Postma and Kleverlaan, 2018; Cornard et al., 2020; Scacchia et al., 2024) which would comform to our experiments.

3 Results

3.1 Morphology of deposits

3.1.1 Series 1

Series 1 consists of a single run. The maximum thickness of the resulting deposit in the channel reached 7.5 cm, located 2.2 m upstream of the break of the slope (Figures 2B,C). Minor erosion occurred along the channel margins. This erosion altered the geometry of the channel, increasing its width from 80 cm to about 90 cm (Figure 2A). The lobate deposit formed in the basin is asymmetric and approximately 2.75 m long (Figures 2A,C). The maximum thickness of the lobate deposit is 5.9 cm and located to the right side of the basin floor axis, about 0.55 m downstream from the break of slope. The thickness of the lobate deposit decreases laterally and distally (Figures 2B,C). Ripples formed on the outermost side of the channel axis and in the distal part of the basin floor.

3.1.2 Interpretation

Low sediment concentrations lead to weakly stratified flow, resulting in dilute conditions that promote turbulence and mixing (Baas et al., 2005). In contrast, high sediment concentrations make the flow dense and stratified, which dampen turbulence and mixing (Talling et al., 2012). However, at the sediment concentration used in this study (17 vol. %), the high sediment aggradation in the channel is probably not related to the low flow density but has been caused by low flow competence to move the grains with D_{50} = 148 µm used in the experiments. These coarse grains fractionate and settle more quickly (Middleton, 1993) and promote early deposition and decreased suspended sediment load. The low flow efficiency may also be due to drag forces (the resistance exerted by a fluid on a solid particle passing through it, which oppose the movement of the particle in the flow). These effects caused by a 7.5% concentration of heavy minerals (Wang and Maxey 1993). The asymmetric lobe deposit (Figure 2C) reflects the influence of pre-existing basin floor topography, due to manual sculpting of the sandy substrate, which directed flows and localized sediment accumulation (Soutter et al., 2021).

3.1.3 Series 2

In Series 2, two successive runs were conducted. In Run 1, significant sedimentation was noted in the upper channel, with a maximum thickness of 6 cm, decreasing to 4.2 cm in the lower channel (Figures 3A,C). Negligible overspill was observed and did not form a levee deposits. The channel width expanded from 70 cm to 87.6 cm (Figure 3A). The lobate deposit on the basin floor formed during this run is symmetrical and measures 2.9 m in length (Figure 3B). The maximum thickness of the deposit is approximately 6.2 cm, located about 1.4 m downstream from the break of slope. Its width at 0.35 m downstream is roughly 129 cm and increases to 170 cm at 0.94 m downstream of the slope break.

Similar to Run 1, during Run 2, there was negligible overspill to form a levee deposit, and high sedimentation occurred in the channel. The maximum thickness of the deposit is located in the lower part of the channel, measuring 5.8 cm at 0.44 m upstream of the break of slope. Some erosion is observed on the left flank of the channel, increasing its width from 87.5 cm to 1 m (Figure 3A). The lobate deposit from Run 2 is asymmetrical and measures 2 m in length. It is notably shorter than the deposit formed in Run 1 (Figures 3B,C). The maximum thickness is located on the left side of the deposit, reaching 7.6 cm at 0.95 m downstream of the slope break, whereas the deposit is generally thinner on the right side. The deposit width at 0.35 m downstream is about

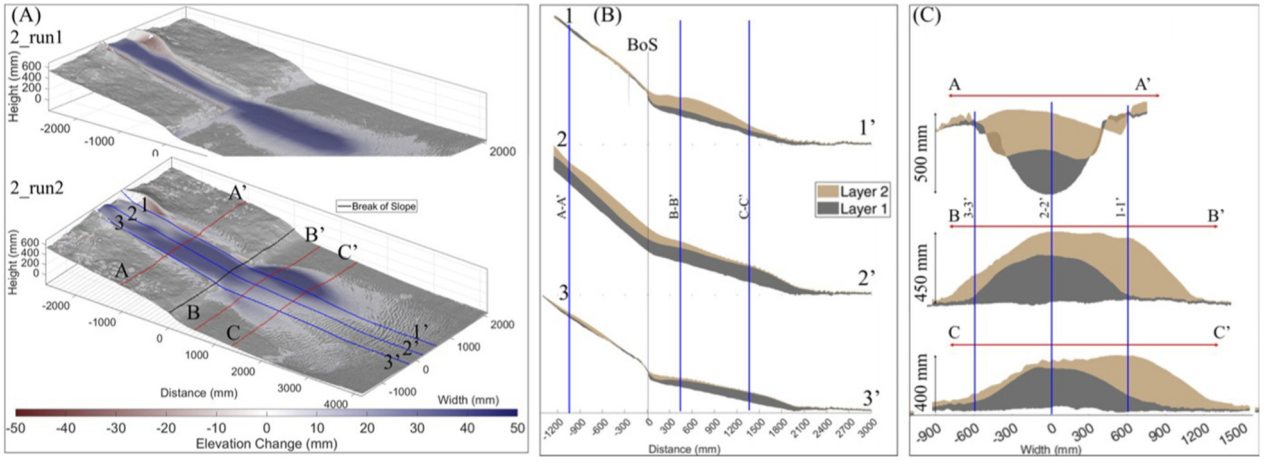


FIGURE 3
Cumulative deposition and erosion maps with cross-section analysis **(A)** Digital elevation models with blue for cumulative deposition and red for erosion (run1-2). **(B)** Dip-sections cumulative deposition and **(C)** Cross-sections with a vertical exaggeration of × 5.

206 cm, widening to 224 cm at 0.94 m downstream of the slope break. Ripples form in the proximal part of the basin floor near the break of slope, mainly towards the right side.

3.1.4 Interpretation

The combination of channel morphology and flow competence influences channel sedimentation and the formation lobate deposits in Series 2. Although the channel width of series 2 is narrower than in Series 1 (Table 1), which favors sediment flow toward the basin floor (De Leeuw et al., 2018), the turbidity current exhibits low flow competence to transport the sediment mixture (D_{50} = 148 μm; high heavy mineral content) toward the basin floor. Therefore, significant sediment accumulation is observed in the channel. The asymmetry of basin floor deposit during Run 2 is due to the avulsion of flow towards the left part of the basin floor caused by the deposit created in Run1, which acts as a topographic barrier (Soutter et al., 2021). As a result, lateral flow steering was favored, transporting sediments to new locations and creating avulsed lobate deposits. This led to the formation of a short, thick composite basin floor lobe (Figure 3).

3.1.5 Series 3

Four consecutive runs were conducted in Series 3. In Run 1, a significant amount of sediment was deposited in the channel, resulting in a thick deposit of about 5.2 mm located approximately 2 m upstream of the slope break. There were negligible overspills of the flow in the slope channel to form a levee deposit. Some erosion was observed on the lower parts of both channel margins, which widened the channel from 70 cm to 93 cm (Figure 4A). After leaving the channel confinement at the break of slope, the flow deposited its load in the center of the basin floor and form a 3.5 m long and symmetrical lobate deposit (Figures 4B,C). Its maximum thickness is 7.6 cm at approximately 1.35 m downstream of the break of slope.

Low deposition was observed in the upper part of the channel during Run 2, whereas high deposition was observed in the lower part of the channel with a maximum thickness of about 7.1 cm at 1.2 m upstream of the break of slope. Erosion of the upper channel on both sides of the flank results in an increase in channel width of up to 1 m. The scour on the right side of the channel diverts the flow to the left side of the basin floor (Figure 4A). The depocenter of the lobate deposit, which is 8 cm thick at about 0.85 m downstream of the break of slope, is on the right side of the basin floor. The length of the lobate deposit is 2.4 m, which is shorter than the deposit of Run 1. Its width is 186 cm at 0.35 m downstream and 210 cm at 0.94 m downstream from the slope break.

In Run 3, low sedimentation was observed in the upper part of the channel, accompanied by minor erosion. Higher sedimentation occurred in the lower part of the channel. Erosion altered the channel width to 1.2 m in the upper section. In the lower part of the channel (near the break of slope), the flow overspills the confines of the channel and deposited sediment onto the overbank area without forming a levee. During this process, the channel pathway became completely filled with sediment (Figures 4, 5A, B). The maximum thickness of the deposit in the channel is 8.8 cm, located 1.1 m upstream from the break of the slope (Figure 4C). The lobate deposit formed during Run 3 is asymmetrical in shape and has a maximum thickness of 5.0 cm on the right side of the basin floor, 0.85 m from the break of slope. At 1.8 m, the length of the deposit is shorter than in the previous two runs. Its width is 243 cm at 0.35 m downstream, decreasing to 178 cm at 0.94 m downstream of the break of slope. A scour developed on the left-hand side of the deposit at 0.6 m downstream of the break of slope.

Run 4 featured significant sedimentation within the channel and considerable overspill. However, no levee deposition was observed; instead, a wing-like structure was deposited on the overbank after the channel completely filled with sediment (Figures 4A,C). The maximum thickness of this deposit in the channel is 11 mm, located 1.2 m upstream of the break of slope. Only a small amount of sediment reached the basin floor, forming a short basin floor deposit measuring 1.2 m in length. The thickness of the basin floor deposits has decreased, with its maximum deposit reaching only 1.2 cm at

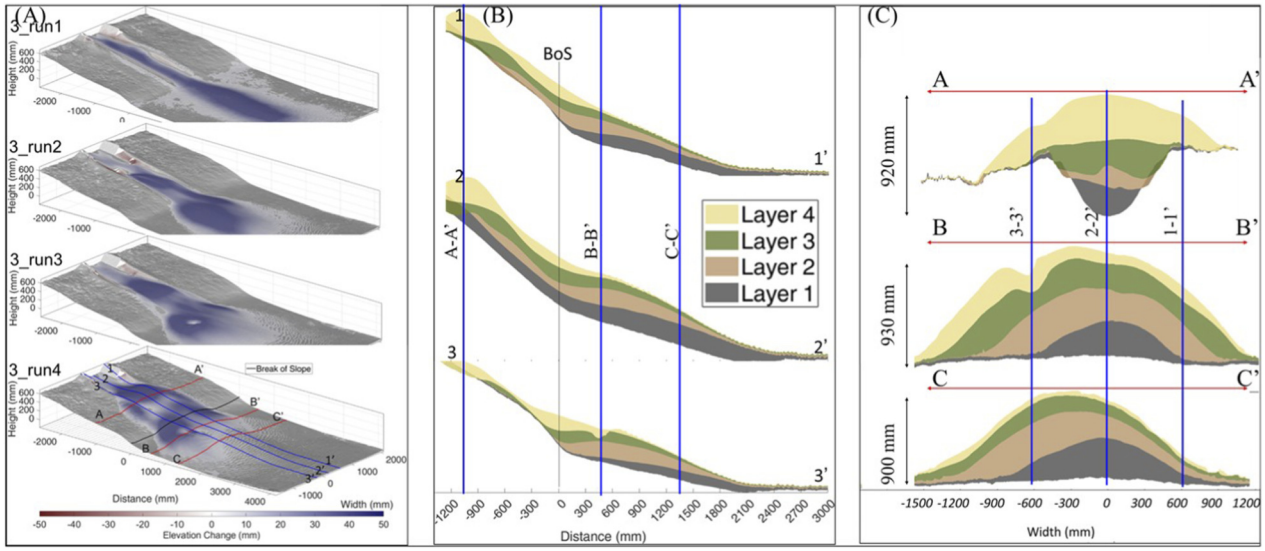


FIGURE 4
Cumulative deposition and erosion with dip- and cross sections. **(A)** Digital elevation models with blue for cumulative deposition and red for erosion of the channel during run1-4. **(B)** Dip-sections and **(C)** Cross-sections cumulative deposition with a vertical exaggeration of ×5.

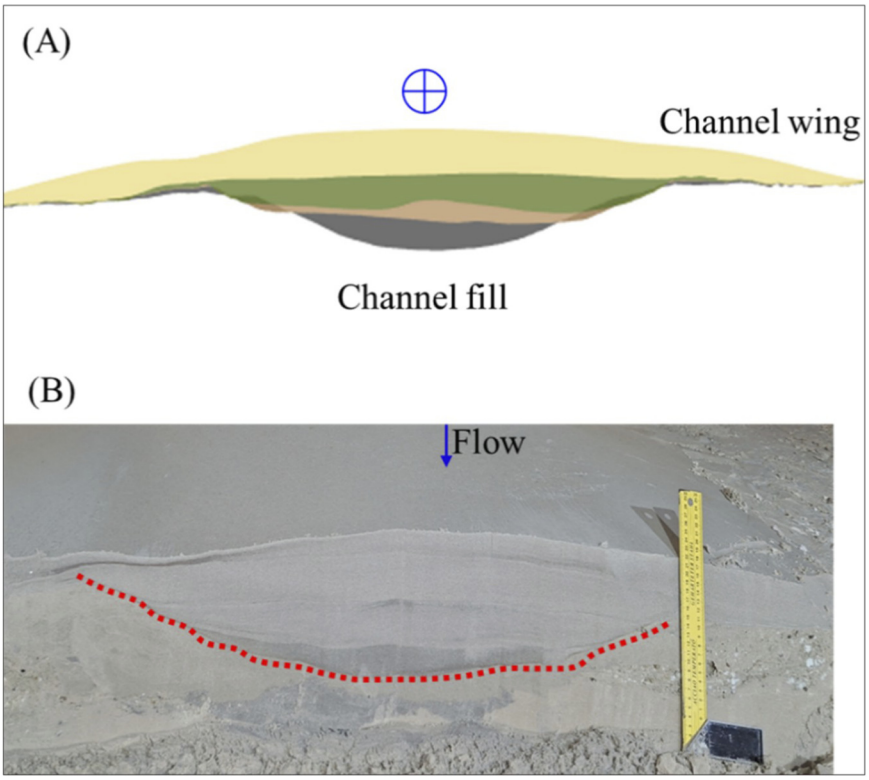


FIGURE 5
(A) Lateral cross-section at the lower channel for four runs that show the channel wings in layer 3 and 4. The circled cross indicates the direction of flow. This cross-section is located at line A-A′ in A. **(B)** Close-up of a photo of the lower channel showing the fill of the canal and amalgamations. The blue arrow indicates the flow direction and the red dotted line shows the geometry of the preformed channel with a width of 70 cm and a depth of 8 cm.

a distance of 0.55 m from the break of slope on the right side of the scour formed in run 3 (Figure 4A). The width of the deposit measures about 259 cm at 0.35 m downstream and decreases to 197 cm at 0.94 m downstream of the slope break.

3.1.6 Interpretation

The depositional patterns of each run in Series 3 were quite different in terms of channel sediment retention, overbank, and basin floor deposition. In runs 1 and 2, channel sedimentation was relatively low compared to Series 1 and 2. This indicates that the turbidity current has high flow competence, enhancing its ability to transport coarser materials (D_{50} = 146 μm) to the basin floor. This results from the increase in sediment concentration from 17 vol. % to 19 vol. %, which increased flow density (Baas et al., 2005; Talling et al., 2012) and enhance sediment transport to the basin floor (Spychala et al., 2020). The heavy mineral content is also decreased from 7.5% to 3% in this series, which would have reduced the drag force on the flows. In Runs 3 and 4, the channel experienced high sedimentation combined with frequent overbank deposition, causing the creation of channel wings (Elliott, 2000) (Figures 4A, 5). In Run 1 of series 3, the lobate deposit on the basin floor was longer and more symmetrical due to increased sediment transport compared to series 1 and 2 due to the increase in the sediment concentration to 19% C_{vol} and reduction of heavy mineral content. During Run 2, increased lateral flow dispersion resulted in shorter, wider lobate deposit. In Runs 3 and 4, channel sedimentation increased, which decreased sediment flux to the basin floor, causing an increase in the width-to-length ratio. The decrease in sediment supply to the basin gradually caused the deposit to become thinner and shorter. However, the deposit width increased due to improved lateral flow distribution (Figure 7).

Scour marks on the channel bed and basin lobe suggest localized erosion, likely formed by shear stresses (Wynn et al., 2002) accumulated in high-velocity regions (Lamb et al., 2008). This erosion can migrate, deepen, and fill with silt over time (Straub and Mohrig, 2009). Nevertheless, at these scours, during Runs 3 and 4, there are no significant changes in flow velocity that resulted in scour formation, nor did they occur at the channel axis due to flow relaxation (Pohl et al., 2020). The scours were likely caused by the instability and slumping of a highly porous sediment layer (Li et al., 2021) or of megaflutes caused by concentrated sediment-laden flows (Elliott, 2000) (Figures 6A,B).

3.2 Flow properties

The turbidity current measurement was taken from the left to the right of the basin floor at intervals of 40 cm (Figure 1B). In this section, the flow velocity of each of the three series is analyzed. Within the body of the current, the velocity increases from zero at the bottom to a maximum value (Umax) at hmax before decreasing to zero at a distance ht. The velocity profiles exhibit a reverse flow (return flow).

3.2.1 Series 1

In Run 1 (Series 1), a high velocity core was measured. The maximum downslope velocity was 0.6 m/s at the center of the basin floor. The lateral velocity decreased to 0.53 m/s at −0.4 m, 0.4 m/s at −0.8 m, and 0.26 m/s at −1.2 m on the right side of the basin floor (Figure 8B). On the left, it decreased from 0.51 m/s to 0.3 m/s between 0.4 and 0.8 m. The maximum lateral velocity was 1.75 m/s on the right side of the basin floor at 0.8 m from the base of slope, and it had the same shape and orientation as the downslope velocity. However, on the left side, the lateral velocity decreased and formed an inverted profile relative to the right side (Figure 8A). The vertical velocities were mostly uniform, showing no prominent differences (Figure 9). Overall, the high velocity core was concentrated near the bottom and along the central axis, decreasing continuously both upward and laterally on the basin floor. This distribution resembled a bell-shaped profile (Figure 8A), characteristic of flow velocity profiles of many turbidity currents.

3.2.2 Series 2

During Run 1, the maximum time-averaged downslope flow velocity is 0.56 m/s at the basin floor axis. To the right side of the basin floor, it decreases to 0.48 m/s at −0.4 m, then successively to 0.38 m/s at −0.8 m and to 0.21 m/s at −1.2 m from the basin floor axis. The downslope current velocity also decreases towards the right side of the basin floor's center from 0.4 m/s at 0.4 m−0.22 m/s at 0.8 m (Figures 8A, 9). The lateral velocity of the turbidity current on the left side of the basin floor follows a trend similar to the downward velocity. On the right side, it exhibits a reversed trend, reaching a maximum velocity of 0.15 m/s at −0.8 m (Figures 8A, 9A). The vertical velocity of the turbidity current shows no significant variation (Figure 8C). The downslope flow velocity in Run 2 is lower than in Run 1. The maximum velocity in Run 2 is 0.53 m/s, shifting to the left side of the basin floor to 0.4 m from the center (Figures 8B, 9). Similar to Run 1, the lateral current velocity in Run 2 follows the same trends on the left side of the basin floor but shows opposite trends on the right side (Figure 8A). The vertical current velocity in Run 2 is higher than in Run 1, showing less variation across the basin floor (Figure 8C). Figure 8D shows the direction of the turbidity current. 0° indicates purely downward flow, while ±90° purely lateral flow. Direction values are negative, reflecting leftward flow, and positive (rightward flow) reflect rightward flow, with the largest deviation on the far left. Direction values also vary with depth. Runs in Series 2 have larger lateral deviations than the run in Series 1, with some variability between runs in Series 2 (Figure 8A).

3.2.3 Series 3

In Run 1, the maximum downslope current velocity is 0.8 m/s at the center of the basin floor axis. It decreased laterally to the right, as observed for Run 1 in Series 1 (Figures 10, 11B). The maximum lateral current velocity is 0.15 m/s at 0.8 m. The patterns of this velocity display the same trends as the downslope velocity (Figures 10, 11A). The vertical current velocity displays a sharp upward peak at −0.4 m, followed by an upward flow near the surface, then slightly bends downward at −0.8 m. At 1.2 m, the velocity is mainly downward (Figure 11C).

During Run 2, the turbidity current velocity was not observed on the right side of the basin floor at 0.8 m from the center because the

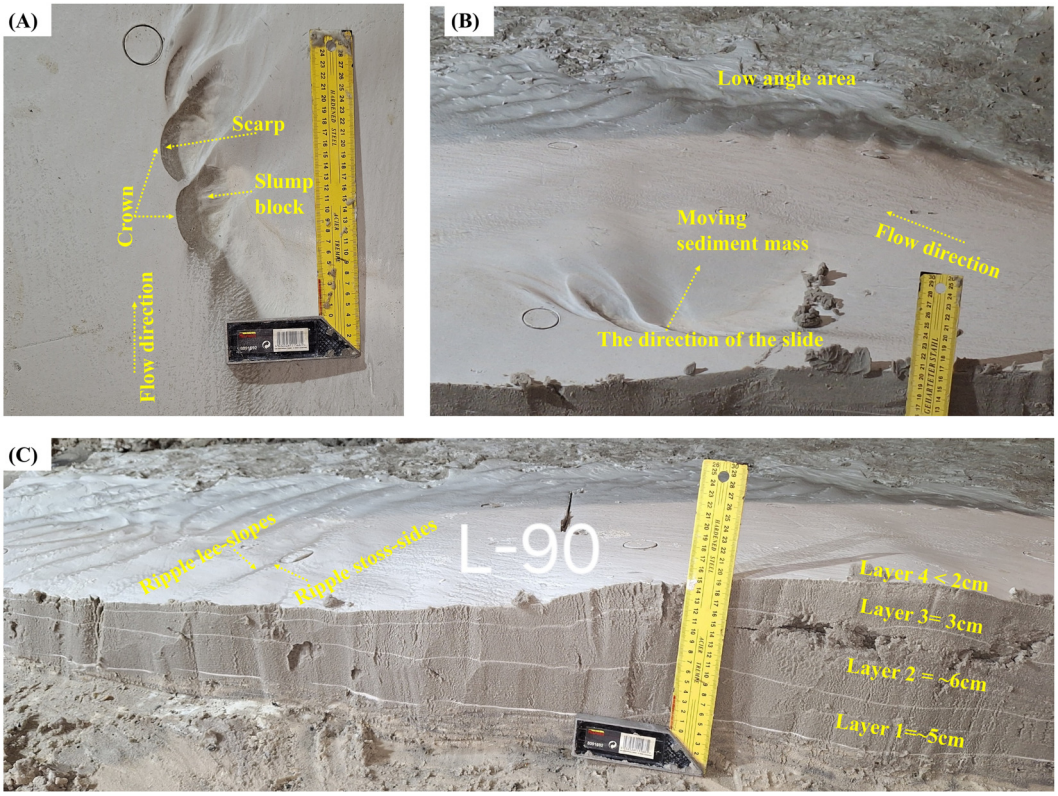


FIGURE 6
(A) Close-ups of the scours showing details of sediment sliding **(B)** Location of the scours approximately 0.6 m downstream of the slope break **(C)** Longitudinal cross-section at 90 cm from the central axis of the channel showing lobate deposits with an upward decrease in bed thickness thicknesses demonstrating backstepping stacking patterns. Note ripple formation on the more distal part.

velocity measurements started too late. The maximum downslope flow velocity is 0.52 m/s and is again located along the basin floor axis; however, this value is lower than the downslope velocity observed in Run 1. The downslope flow velocity decreases laterally as one moves away from the high-velocity core of the flow (Figures 10, 11B). The lateral flow velocity on the right side of the basin floor exhibits the same trends as the downward flow velocity, with its maximum value of 0.25 m/s at −1.2 m (Figures 10, 11A). The vertical current velocity also shows similar trends to the downward flow velocity, with downward flows (Figure 11C).

In Run3, the maximum downslope flow velocity of 0.42 m/s can also be observed at the basin floor axis and decreases laterally. Its overall velocity has decreased in comparison to the currents observed in run 1and 2 both. (Figures 10, 11B). The lateral flow velocity exhibits the same trends as the downslope velocity on the right side of the basin floor with maximum value of 0.15 m/s at −0.8 m (Figures 10, 11A). The vertical flow velocity peaks on the right side of the basin floor at 0.8 m from the center, with a maximum value of 0.043 m/s. It exhibits similar trends to the downward turbidity current with downward flow (Figure 11C).

Both, the downslope and lateral flow velocities in Run 4, were lower compared to the previous runs. The maximum downslope flow velocity is 0.4 m/s, while the lateral flow velocity is less than 0.2 m/s and exhibits the same trends as the downslope flow velocity on the right side of the basin floor (Figures 10, 11B). The maximum vertical flow velocity is 0.04 m/s at −0.8 m to the left of center. It exhibits similar trends to the downward flow velocity and flows downward (Figure 11C). As shown in Figure 11D, the left positions are aligned by negative angles that direct the flow to the left, while the right positions have positive angles and direct the flow to the right, with the most significant deviations on the far right.

3.2.4 Interpretation

The combined velocity profiles from the three series indicate that the variability of turbidity currents is strongly influenced by basin floor morphology and deposition. In Series 1, the flow velocity decreased both laterally and vertically, creating a bell-shaped distribution. This pattern indicates a gravity-driven, densely stratified flow concentrated near the bed and consistent with classic turbidity current behavior (Middleton and Hampton, 1973).

As build-up of the system progressed, deposition led to the formation of topography responsible for the re-routing and lateral displacement of the flow core (Series 2) (Figure 9). This evolution of the flow field is associated with the development of rectangular velocity profiles in Run 2 of Series 2 at −0.4 m and 0 m, which differ from the classic turbidity current velocity profile (Figure 8A). Flow field evolutions are essential for maintaining balanced lobe growth and widespread sediment distribution across the submarine fan systems. The reduction in overall velocity

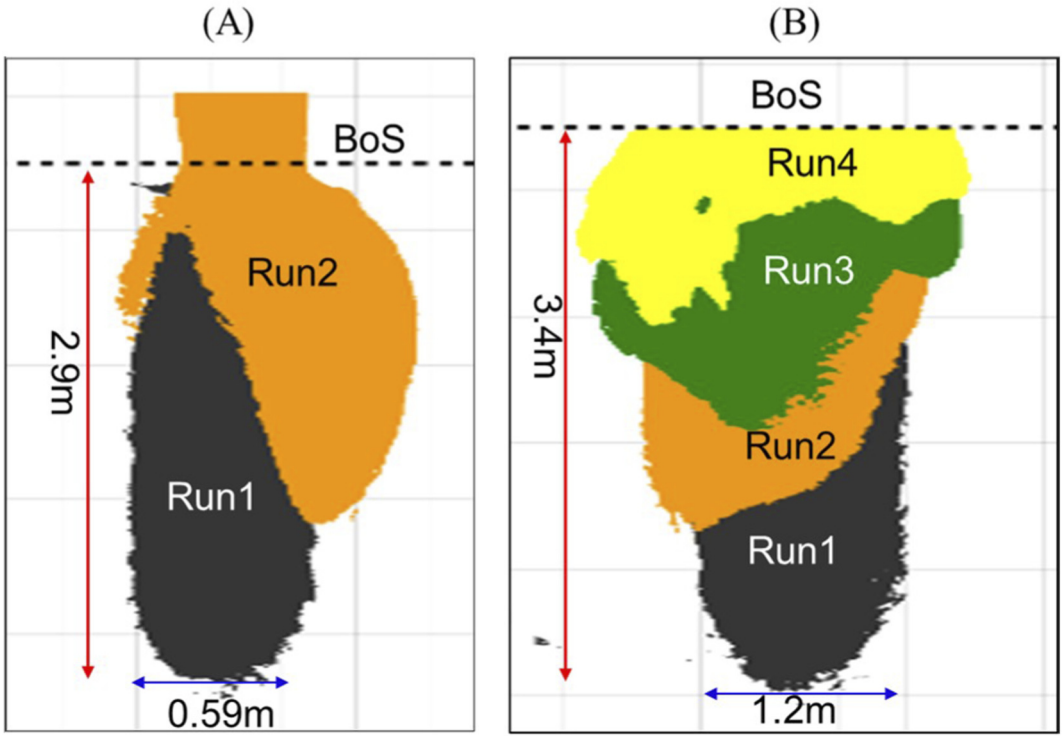


FIGURE 7
(A) Lobe deposit of Series 2 showing compensational stacking and avulsion, and **(B)** Lobe deposit of Series 3 demonstrating anti-compensation and backstepping.

reflects the influence of topographic barriers impeding the flows (Talling et al., 2012; Soutter et al., 2021).

In each successive run of Series 3, the downslope current velocity decreased while the lateral velocity increased (Figures 9, 10), reflecting a reduction in the central current's momentum and an increase in lateral dispersion. This behavior can be attributed to progressive sedimentation in the channel, which reduces the current's energy and limits its movement toward the basin floor and thus promotes lateral dispersion (Parker et al., 1986; Meiburg and Kneller, 2010; Hitomi et al., 2021).

3.3 Sediment volume distribution

3.3.1 Series 1

In Series 1, the volume of sediment in the channel exceeds that of the basin floor deposits (Figure 12). About 82.4 L (54%) of the total 153 L of sediments is deposited in the channel. In this series, the flow is contained within the channel without overspills and levee deposits. The remaining sediment, about 70.6 L, passed into the basin to form a lobate deposit (Figure 12A).

3.3.2 Series 2

In Series 2, changing the slope gradient of the channel from 9° to 12.5° (in comparison to Series 1) altered the sediment distribution. Initially more sediment was transported to the basin floor. During Run 1, about 97.5 L (64%) of the total sediment of 153, passed into the basin to form a lobate deposit. Only 36% of the sediment was deposited in the channel (Figure 12B). Run 2 shows a similar high aggradation in the channel as Run 1 in Series 1. In Run 2, 73.3 L (48%) of the total sediment deposited on the basin floor. 52% of the sediment was deposited in the channel (Figures 3A, 12B).

3.3.3 Series 3

During Run 1, 48.6 L (28%) of the total sediment volume of 171 L was deposited in the channel, whereas 72% (122.4 L) of the sediment were deposited on the basin (Figure 12C). In Run 2 33.6 L of sediment deposited in the channel, which is 20% of the total sediment. 173.4 L (80%) of the sediment was transferred to the basin. Thus, the volume of sediment in the basin during Run 1 and 2 exceeds the volume of sediment in the channel. (Figure 12C). However, a different pattern was observed in the two remaining runs.

In Runs 3 and 4, sedimentation increases significantly in the channel. During Run 3, 92.7 L (54%) of the total sediment was deposited in the channel, with some sedimentation on the overbank area. 46% of the sediment was deposited on the basin floor. During Run 4, 75% (128 L) of the sediment was deposited in the channel and as overbank deposits, whereas only 25% of the sediment reached the proximal basin. Overall, the volume of sediment in the basin for Runs 3 and 4 is less than the volume of sediment in the channel (Figures 4A,C, 12C).

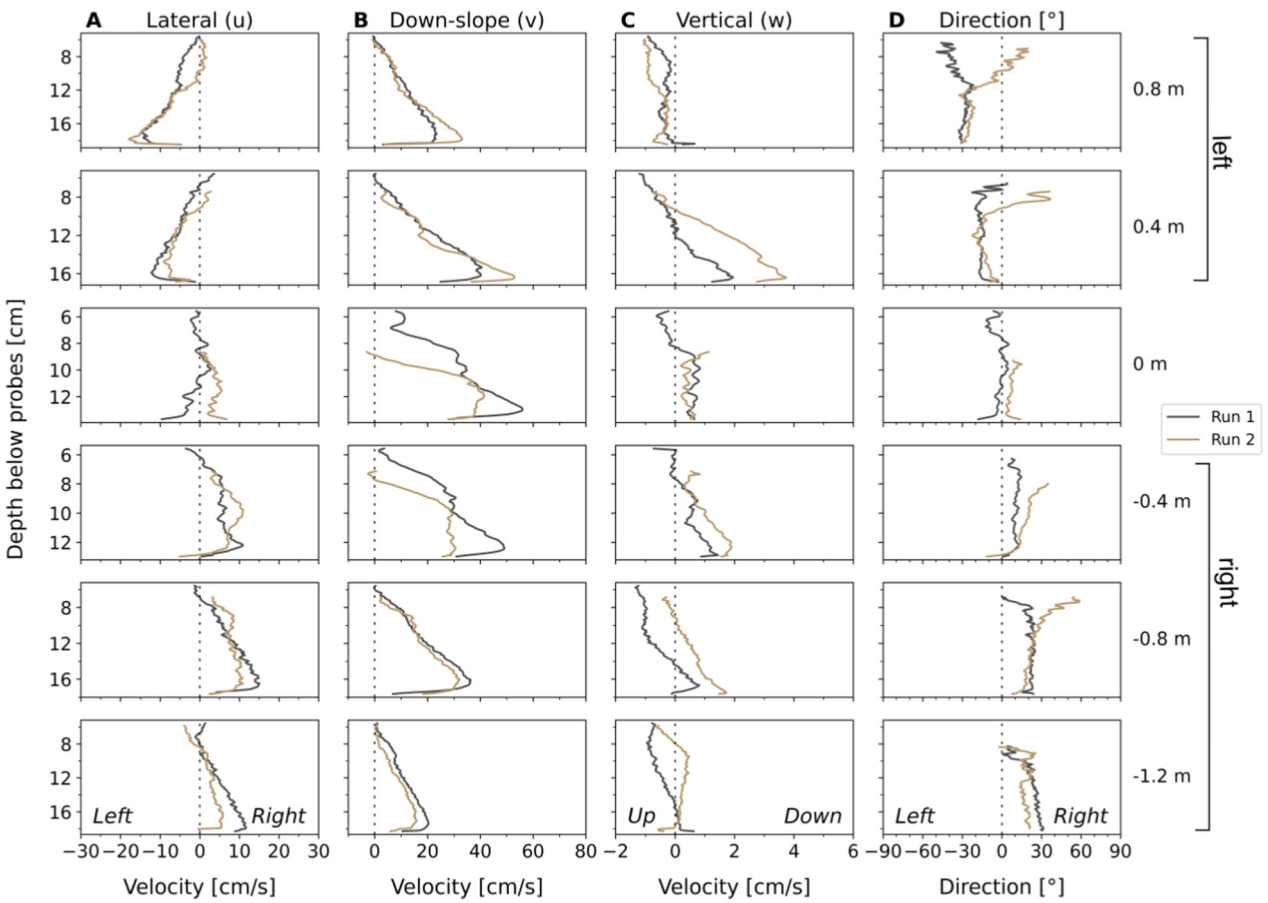


FIGURE 8
Shows the time-averaged velocity profiles **(A–C)** and turbidity current direction **(D)** of Series 2. Depths in each subplot correspond to the profile with the maximum depth. Data were collected at six positions with 40 cm intervals, and no data is available for position 1.2 m (left). Dotted lines are plotted at x = 0. **(A)** Lateral velocity profiles, where negative velocities indicate leftward flow and positive velocities indicate rightward flow. **(B)** Down-slope velocity profiles, where negative values represent back-flow and positive values indicate a down-slope direction. **(C)** Vertical velocity profiles, where positive values indicate downward flow and negative values indicate upward flow, the absolute numbers of which are likely exaggerated. **(D)** Direction of the turbidity current, calculated from the down-slope and lateral velocity components. At 0°, the lateral component is zero, while at –90/90°, the down-slope component is zero.

3.3.4 Interpretation

The high aggradation in the channel in Series 1 is explained by the high mineral concentration and grain size of the sediment mixture (D_{50} = 148), which resulted in increased retention and decreased sediment transfer. In addition, the related low flow competence and limited flow capacity likely promoted sedimentation in the channel, resulting in reduced sediment delivery to the basin floor (Hiscott, 1994). In Series 2 and 3, the channel width was narrowed to 70 cm, with sediment concentration increased in Series 3. These changes were made to ensure enough sediment was transported into the basin at the start of the series of successive runs. As the topography of channel evolved, more sediment was deposited in the channel compared to the basin floor, especially during Run 3 and 4 (Figure 12C). It demonstrates how changes in channel geometry (De Leeuw et al., 2018) and increased sediment concentration (Spychala et al., 2020) can impact sediment transport and deposit morphology.

3.4 Stratal stacking patterns of channel deposits and basin floor deposits

Here stacking patterns for Series 2 and 3 are presented. Series 1 has not been considered because it consists of only one run.

3.4.1 Series 2

During Run 1, initially a deposit formed that prograded into the basin floor. The deposit of Run 1 was subsequently partially overlain by the deposit of Run 2 (Figure 7A), which overall shows a backstepping pattern as well as avulsion of the depocenter to the left-hand side of the basin floor. In cross section (Figure 3C) this pattern can either be expressed as aggradational in the channel (line A-A′), aggradational to slightly compensational stacking patterns in the proximal part of the basin floor (line B-B′) or as compensational stacking further into the basin floor (line C- C″).

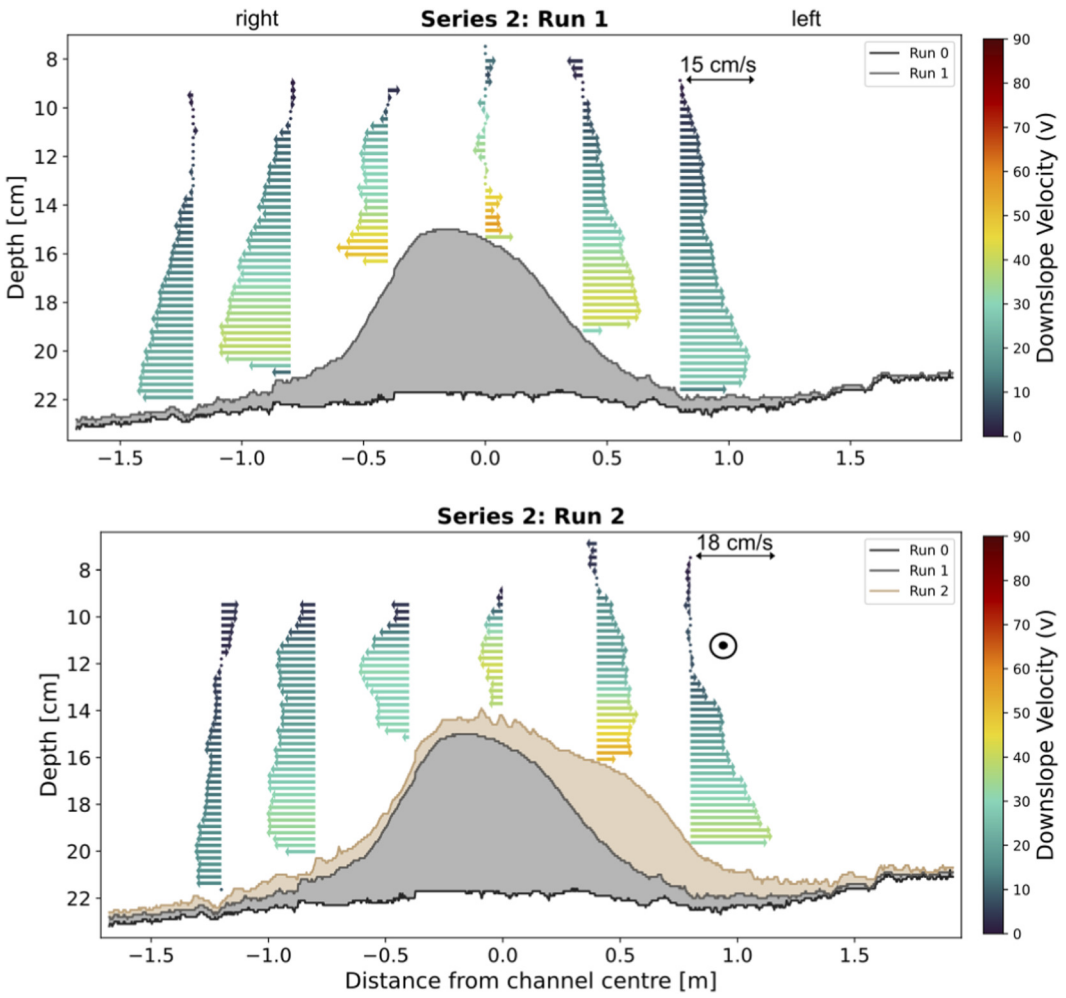


FIGURE 9
Cross-sections illustrating turbidity flow structure above the bed in Series 2, Runs 1 and 2. The cross-section is located 1.75 m downstream of the slope break. Lateral velocities are represented by vector length, while down-slope velocities are depicted by the color bar. Since measurements were taken during deposition, the depths of the velocity profiles were slightly adjusted to align with the bed.

3.4.2 Series 3

Overall, the deposit in Series 3 demonstrates backstepping along with minimal avulsions of the depocenter to the right side of the basin floor (Figure 7B). During Run 1, the experimental turbidity flow resulted in deposits that prograded into the basin floor. This initial deposit was followed by subsequently backstepping deposition of runs 2, 3 and 4. The cross-section clearly illustrates these lateral and vertical depositional patterns (Figure 4C). Sediment accumulation is predominantly aggradational (line A-A′) in the channel. In the proximal region of the basin floor, the pattern changed from aggradational to slightly retrogradational stacking patterns along line B-B′ and completely retrogradational patterns along line C-C′ in Figure 4.

3.4.3 Interpretation

The stacking patterns observed in Series 2 resulted from flow dynamics. The compensational stacking pattern is due to flow deflection by sediment previously deposited during the Run 1 (Figures 3, 7A). The backstepping stacking pattern is attributed to low sediment bypass into the basin floor. In Series 3, various stacking patterns are observed, ranging from aggradation to retrogradation, with no progradational stacking patterns (Figures 4, 6C, 7B). The absence of progradational stacking in Series 2 and 3 indicates that flow efficiency was insufficient to transport sediment further into the basin. This low flow efficiency is believed to result from the high amount of sediment in the channel, leading to increased friction and energy dissipation (Catuneanu et al., 2006; Payros and Victoriano, 2008).

4 Discussion

4.1 Hierarchy of depositional elements in submarine fans

In natural submarine fan systems, the hierarchy of depositional elements progresses from a single bed to lobe elements, then to lobes and lobe complexes. A lobe element is formed by a combination of

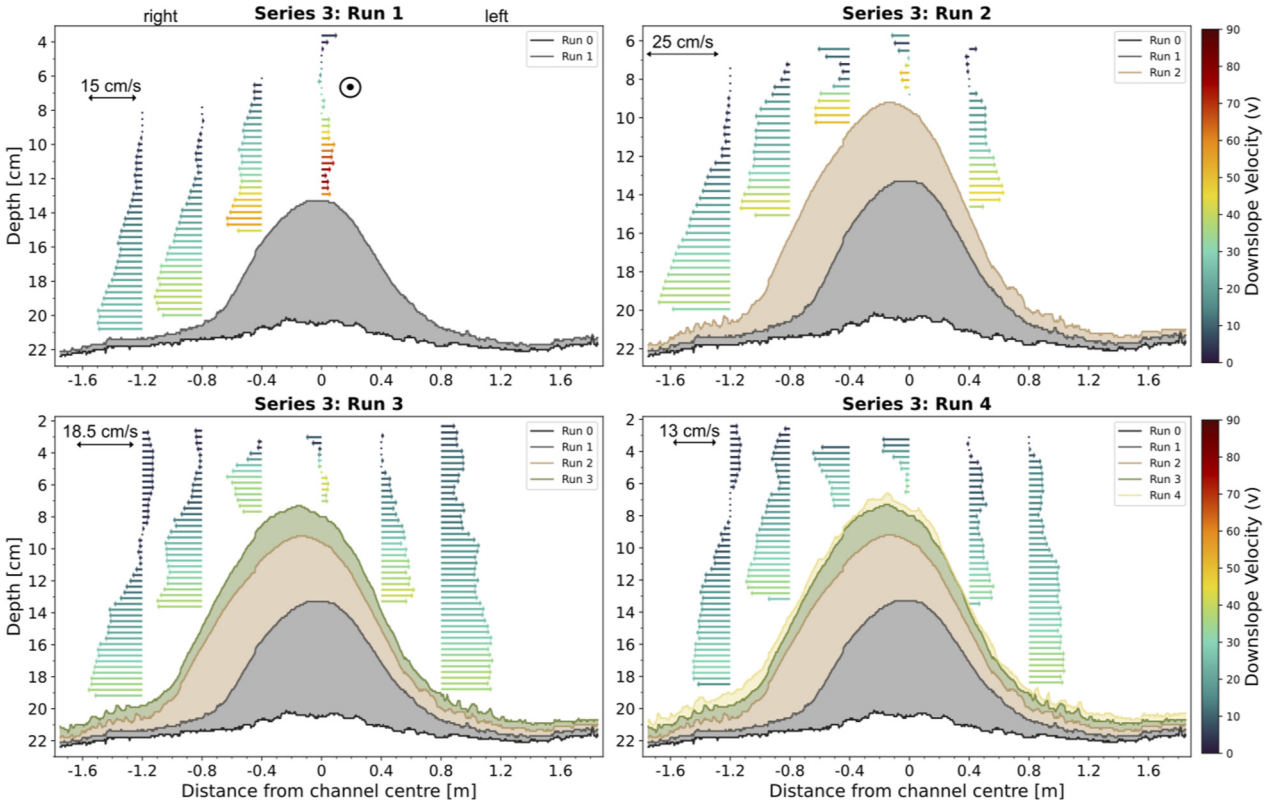


FIGURE 10
Cross-sections illustrating turbidity flow structure above the bed in Series 3, Runs 1 to 4. The cross-section is located 1.75 m downstream of the slope break. Lateral velocities are represented by vector length, while down-slope velocities are depicted by the color bar. Since measurements were taken during deposition, the depths of the velocity profiles were slightly adjusted to align with the bed.

stacked beds. Deposits created during single run turbidity current experiments are thought to typically reach to the level of lobe elements (Figure 7) (Spychala et al., 2020). This conforms to the idea of Straub and Pyles (2012) who state that compensational stacking is less pronounced at lower hierarchical levels. A lobe is a composite body formed by the stacking of lobe elements (e.g., Hodgson et al., 2016; Spychala et al., 2020). Subsequent runs conducted in Series 2 and 3 represent the build-up of a single lobe by several lobe elements, that show more varied stacking patterns than those produced by simple aggradation.

4.2 Autogenic flow field evolution and its effect on sediment retention in the channel and basin floor deposits

The typical velocity profiles of turbidity current created in the experiments are presented in Figures 8, 11. The velocity near the bed is close to zero, increases to a maximum at a specific height above the bed, and then decreases towards the top of the flow. Except for Run 2 in Series 2 and 3, the velocity profiles in all series exhibit a classical velocity profile shape (bell-curve). Negative velocities in the flow at the centre of the basin floor in Series 3 tend to move backward flow due to the shear force between the turbidity current and the surrounding water (Figure 11). This is consistent with the work of Alves et al. (2008) and Alves and Rossatto (2011).

The resulting velocity profiles highlight the complexity of turbidity current behavior and their evolving interaction with basin floor topography. It is important that the deviation from the classical profile in the second runs of series 2 and 3 (Figures 8, 11) may result from significant changes in flow structure (the internal organization and dynamics of the turbidity current) due to morphodynamic feedback. Such modifications stem from the deflection of flow by pre-existing deposits, which alters sediment distribution patterns and thus the geomorphology and architecture of the lobe deposits. The high flow velocity at the center of the basin floor enhanced sediment transport efficiency along the central core and created elongated deposits during the first run of series 2 and 3 (Figure 7). These observations align with single run simulations by Spychala et al. (2020) and Bell et al. (2021).

However, the smooth and simple dynamics cannot continue indefinitely in successive runs of Series 2 and 3. A significant internal reorganization occurs as the flow begins to pass over the break of slope. The Series 2 results indicate that avulsion happens within the turbidity current system. However, this avulsion does not imply a complete transfer of sediment transport toward the avulsed direction. What occurs is not a complete shift of the flow field, but rather the high-velocity core of the flow, which carries most of the sediment, moves to a new location. Despite this shift, sediment does not solely deposit along the avulsed pathway. Deposition is still occurring across the already formed

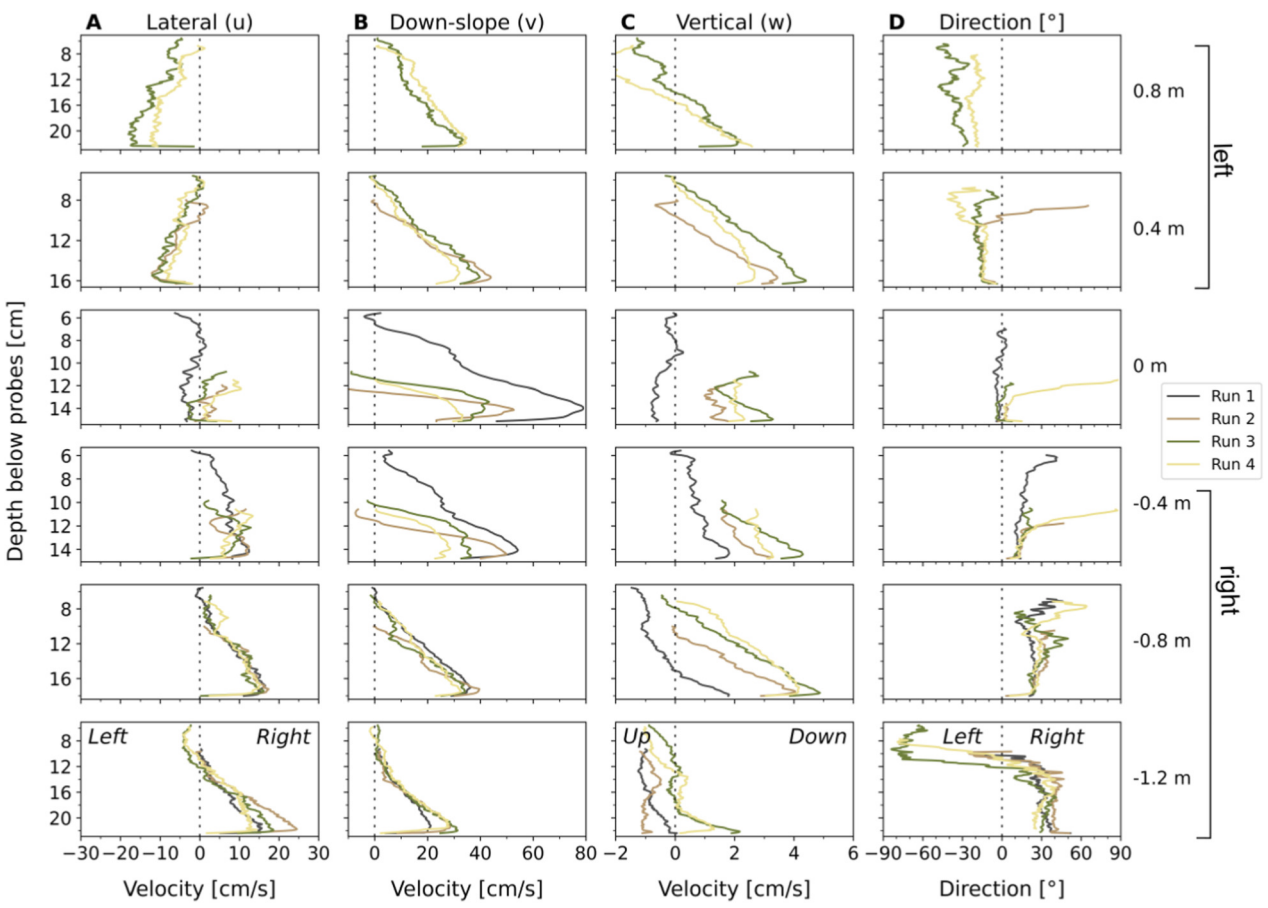


FIGURE 11
Time-averaged velocity profiles **(A–C)** and the direction of the turbidity current **(D)** for Series 3. The depths in each subplot correspond to the profile with the maximum depth. Data were collected at six positions at 40 cm intervals, with no data available for position 1.2 m (left). Dotted lines are plotted at x = 0. During Run 1, no data were recorded on the left side of the basin floor. **(A)** Lateral velocity profiles, where negative velocities indicate leftward flow and positive velocities indicate rightward flow. **(B)** Down-slope velocity profiles, where negative values reflect back-flow and positive values signify a down-slope direction. **(C)** Vertical velocity profiles, where positive values denote downward flow and negative values indicate upward flow. The absolute values of these are likely exaggerated. **(D)** Direction of the turbidity current, computed from the down-slope and lateral velocity components. At 0°, the lateral component is zero, while at −90/90°, the down-slope component is zero.

topography if less rigorously. Thus, other slower parts of the flow remain active in building the deposit in areas outside the main avulsion path (Figures 7, 9). The offset of the flow field may have caused the subsequent turbidity current to divert to the left, adhering to the principle of preferential deposition in topographic lows (Piper and Normark, 1983; Middleton and Southard, 1984; Straub et al., 2009; Ferguson et al., 2020). The second explanation is that the avulsion was triggered by morphodynamic processes. Hamilton et al. (2015) noted that in supercritical turbidity-current experiments, deposition (mouth-bar and lobe formation) and backfilling can block or slow the original flow path. This causes flow stagnation and eventual avulsion into a new channel, which reduces the efficiency of the original flow path over successive events. In natural settings (Deptuck et al., 2007; 2008) and experimental studies (Hamilton et al., 2015; Ferguson et al., 2020), aggradation often precedes back-stepping. However, if avulsion was indeed triggered by morphodynamic processes, excessive channel fill may have impeded the development of an aggradational phase in the basin floor.

The flow velocities measured in Series 3 along the basin floor decrease continuously across successive runs (Figures 10, 11 at 0.0.4, −0.4 m). While the high-velocity core along the basin floor's central axis dissipates, the lateral spreading of the flow persists (Figure 10), leading to the formation of wider, thinner and shorter basin floor deposits (Figure 7). This transition from a jet-like to a laterally expanding flow results in varying stacking patterns across the basin floor deposits. The vertical stacking pattern and lateral shift observed in the deposits show a degree of spatial variability that characterizes changes in flow and sedimentation processes throughout the basin floor.

In Run 2 of series 3, scour formations developed in the upper channel, altering the flow to the left and causing deposition away from the center of the basin floor axis (Figure 4A). This illustrates the effects of morphodynamics on sediment bypass and lobe formation. Scour formation caused by substrate irregularities is common in nature (Hay and Speller, 2005), and both modern and ancient evidence of channel and lobe scours is also prevalent (Casagrande et al., 2024).

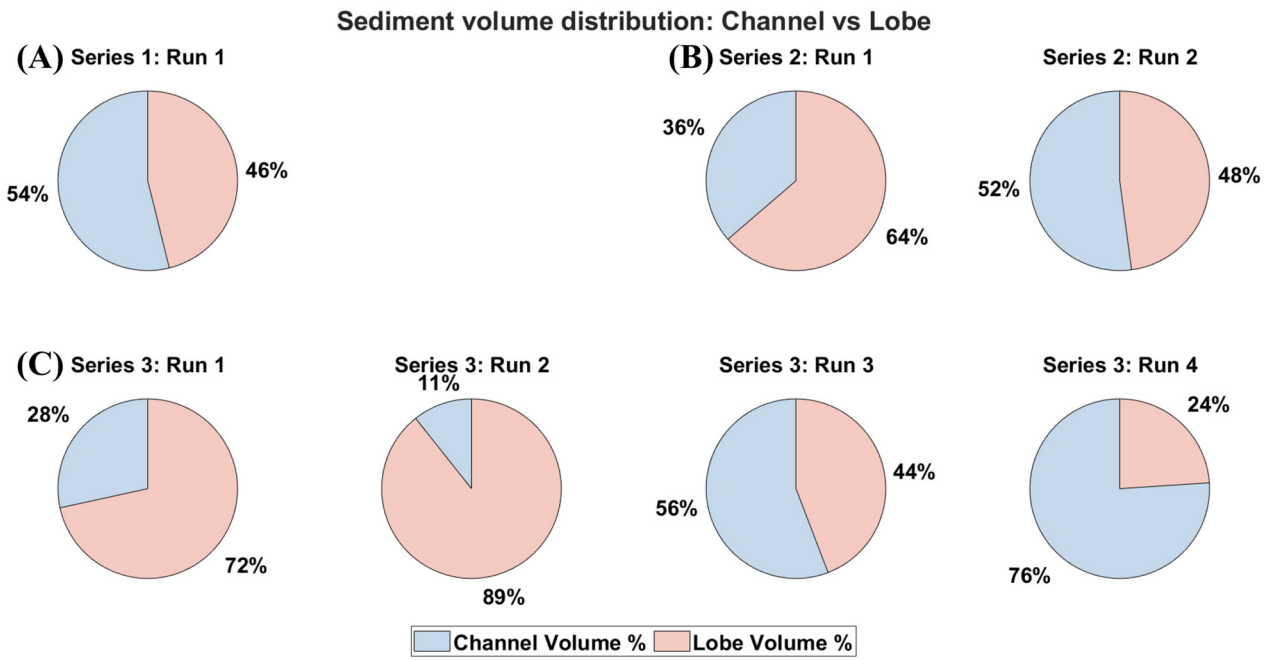


FIGURE 12
Sediment volumes of an experimental run (blue for the channels and red for the lobes). **(A)** Series 1 with sediment concentration of 17 vol%. **(B)** Series 2 with sediment concentration of 17 vol %l. **(C)** Series 3 with sediment concentration of 19 vol%.

The sediment concentration (17 vol.%) and heavy mineral content (7.5%) were relatively high, but sediment bypass in series 1 and 2 remained low, unlike other studies (De Leeuw et al., 2018; Ferguson et al., 2020; Spychala et al., 2020; Bell et al., 2021) who observed more efficient sediment transport to the basin floor under similar conditions. Lowered efficiency could be introduced due to limited flow capacity to suspend the amount of sediment in the fluid and limited flow competence to transport the coarser grains to the basin floor (Hiscott, 1994). When the sediment concentration in series 3 increased from 17 vol.% (used in Series 1 and 2) to 19 vol.%, the flow density and basal shear stress increased, thus enhancing the flow competence to transport grains (D50 = 146 μm) to the basin floor. This resulted in an elongated deposit on the basin during Run 1 (Figure 7B). This observation indicates that, in addition to the autogenic controls, changes in sediment concentration can alter the hydrodynamic and morphological configurations of deposition. However, during successive runs, channel sedimentation (settling of coarse grains) increases likely due to a reduction in flow competence probably due to increased bed roughness and sediment accumulation in the channel and morphodynamic feedback. As a result, the basin floor deposits become wider, thinner, and shorter (Figure 7). Therefore, the evolution of turbidity currents in the experimental series shows that autogenic processes, such as morphodynamic feedback, flow deflection, and avulsion play a critical role in sediment distribution and lobe architecture alongside allogenic factors. Changes in flow structure (offset) affect sediment retention in the channel and sediment routing. Variations in sediment concentration also affect flow competence and deposition efficiency. These results highlight the dynamic interactions between flow behavior, topography, and sedimentation in controlling in channel-lobe systems.

4.3 Stacking patterns and architecture of autogenic flow deposits

Submarine lobes can display various stacking patterns, including aggradational, progradational, retrogradational, and compensational stacking (e.g., Prélat et al., 2009; Straub et al., 2009; Prélat and Hodgson, 2013). A combination of allogenic and autogenic processes controls these depositional patterns. An increase in sediment supply is suggested to lead to progradation, whereas a decrease in sediment supply is thought to cause retrogradation (Grundvåg et al., 2014; Hodgson et al., 2016; Grime et al., 2024). However, most authors postulate that compensational stacking indicates the internal organization of lobe deposits (Straub et al., 2009; Ferguson et al., 2020; Spychala et al., 2024).

In this study, lobe equivalent (see Ferguson et al., 2020) experimental deposits were formed under constant boundary conditions; i.e., there was no increase or decrease in sediment supply, flow velocity or volume of the turbidity currents. While partly showing compensational and aggradational tendencies, the dominant stacking pattern observed in Series 2 and 3 (two and four successive runs, respectively) is retrogradational (Figures 6C, 7A, B).

During successive runs of each series, the channel's capacity to transport sediment to the basin floor decreased due to reduced confinement. This caused channel aggradation in Series 2 and 3 and the formation of channel wings during Series 3 (Figures 4, cross sections A-A′ , 5A, B). The formation of these channel

wings and the aggradational channel fills indicate sediment overflow during late channel filling, similar to patterns described by Elliott (2000) in the Ross Sandstone Formation. In the proximal regions of the basin floor, the deposits tend to thicken upward (Figures 3, 4, B-B′). Although these patterns are perceived as signs of lobe progradation (Hodgson et al., 2016), it is essential to note that no progradation was observed in this study. The upward thickening reflects local aggradation and lateral migration of depositional elements caused by autogenic processes rather than basinward lobe progradation. At the distal central axis, the deposits exhibit an upward thinning pattern (Figures 3, 4, C-C′) associated with a decrease in flow energy and sediment supply. This retrogradational, backstepping pattern was caused by channel infilling, suggesting that not all retrogradational stacking patterns reflect waning sediment supply; instead, they could also be an indicator of channel avulsion and establishment of a new lobe depocenter (Deptuck et al., 2007; Sahoo et al., 2020).

The interpretation of retrogradational, compensational stacking patterns and thinning upward trends in natural submarine fans is primarily linked to reduced sediment supply, rising sea levels, and tectonic activity (Catuneanu, 2006; Ferguson et al., 2020). However, backstepping and retrogradational patterns can occur under constant boundary conditions, as demonstrated in this set of experiments. This result suggests that similar patterns in ancient submarine records should not be automatically interpreted as evidence of reduced sediment supply.

The results of our experiments with constant boundary conditions both complement and contrast with several recent experimental and modeling studies on submarine fan evolution. Hamilton et al. (2015) conducted steady-flow salt-density current experiments and reported a full spectrum of progradational, aggradational, and retrogradational stacking. Their setup uses saline underflows, which differ dynamically from our experimental setup (sediment-laden turbidity currents) and did not use discrete run cycles. Most importantly, their experimental setup was designed to develop incised channels, allowing for continuous sediment supply to the lobe domain. Therefore, topographically driven backstepping of lobes occurred, with hydraulic choking located in the basin floor rather than the channel to prevent upstream avulsions that hindered progradation.

Through systematic variation of sediment discharge, Ferguson et al. (2020) achieved progradational, aggradational, and retrogradational stacking sequences. It was observed that the variability in stacking results from controls on sediment supply, which indicates that the stacking patterns in these experiments would not prograde under constant conditions. This supports the theory that progradation may be linked to the influence of allogenic processes rather than autogenic.

Burgess and Duller (2024) utilized Lobyte3D to illustrate emergent complex patterns even in the absence of external influences. Their results indicate that inherited topography significantly affects channel avulsion and lobe deposition, resulting in compensation and retrogradational stacking as feeder channels become increasingly infilled. The simulated depositional events display characteristic lobe features, including lateral migration, recognizable thickness trends, and divergence after the slope break, as observed in our experiments (Figures 2, 4).

The outcomes of the experimental series conducted here provide additional evidence that submarine lobes evolving under constant boundary conditions may not develop progradational lobe stacking patterns. Instead, these lobes are characterized by compensational stacking, aggradation, and retrogradation, indicative of limited lateral channel avulsion and inefficient sediment transfer. Consequently, lobe deposition is closely linked to the morphodynamic evolution of the channel, as well as to sufficient particle transport and basinward progradation, which involves channel efficiency (i.e., the ability of the channel to deliver sediment to the lobe). Channel efficiency generally coincides with episodic external drivers (e.g., relative sea-level fall, increased sediment supply), which lead to slope incision and channel confinement, as described by Hodgson et al. (2016). Such efficiency is maintained by sustained supercritical flows without hydraulic chokes, allowing for effective sediment transport over long distances (Hamilton et al., 2015). Therefore, in this study, none of the experiments conducted within the autogenic process showed signs of lobe progradation, suggesting that progradation is probably related to allogeneic forcing. This hypothesis will be tested in a subsequent set of experiments with varying boundary conditions.

4.4 Distribution of sediment volume in the channel and basin floor deposits

The distribution of sediment volumes in submarine fan systems, such as channel fills, levees, lobes, varies depending on basin floor geomorphology and sediment supply and flow competence (Hiscott, 1994; Ferguson et al., 2020). While sediment supply is often considered the most critical factor, internal morphodynamic processes and flow competence in turbidity currents also play an important role in sediment distribution. Although sediment input was constant in this experimental study, sediment distribution between the channel and lobe deposits fluctuated throughout the experiment (Figure 12). Previous detailed studies (Jegou et al., 2008; Sylvester et al., 2012; Picot et al., 2016; De Leeuw et al., 2018) have documented datasets from outcrop, subsurface, and experimental studies that have shown sediment volume distributions in different submarine fan systems.

Sediment partitioning between channel-levee systems and terminal lobes has been observed in large submarine fans such as the Congo Fan (Picot et al., 2016) and the Amazon Fan (Pirmez and Imran, 2003; Jegou et al., 2008). These studies highlighted how turbidity currents partition sediment differently in confined and unconfined depositional environments. Moreover, subsequent research has shown similar patterns of sediment volume distribution between the submarine slope and the basin floor, highlighting the broader importance of this partitioning in deep-water systems (Carvajal and Steel, 2011; Van Der Merwe et al., 2014; Prather et al., 2017).

The distribution of sediment volume between the channel and basin floor deposits of each series in this study varied depending on channel geometry, morphodynamic feedback and flow efficiency. The channel depth became increasingly shallower after each run in Series 2 and 3, resulting in high sediment retention in the channel. These results are consistent with those of De Leeuw et al. (2018), who found that wide and shallow channels dimensions promote

sedimentation, which determines the volume of sediment available to be deposited in levee and lobe deposits. De Leeuw et al. (2018) observed variability in sediment volume within the channel-levee and lobe deposits and noted that the sediment volume of the lobe is significantly larger than that of the channel-levee system. In contrast to the findings of De Leeuw et al. (2018), the basin floor sediment volume in Series 1, Series 2 (Run 2) and Series 3 (Runs 3 and 4) is lower than that of the channel due to low flow competence and channel evolution as well as flow dynamics (backflow) (Figure 12). In Series 2 (Run 1) and Series 3 (Runs 1 and 2), the relatively higher volume of sediment in the basin floor compared to the volume of sediment in the channel indicates that the channel was relatively efficient in bypassing sediment to the basin floor (Figure 12).

Unlike the work of Straub et al. (2012), who documented the distribution of sediment volumes between channels and levees, negligible sediment volumes in levees were recorded in this study (Figures 2, 3, 4A). This suggests that the flow remained confined within the channel, as reported by Hubbard et al. (2009) and Hubbard et al. (2014). The differences observed between channel and lobe sediment volumes emphasize the strong impact of channel geometry and flow competence and autogenic processes on the depositional architecture. Although the absence of levee development differs from many natural systems and experimental studies, it highlights the importance of flow confinement and flow efficiency in shaping sediment distribution. Therefore, this study enhances our understanding of how internal dynamics influence deep-sea sediment routing and sedimentation.

4.5 Autogenic processes and the interpretation of submarine lobe records

Turbidity currents in the natural environment are affected by waning or surge-type currents, which are controlled by climate and tectonic activity (Kneller and Buckee, 2000; Talling et al., 2012). In our experiments, however, using steady inflow conditions helped to isolate autogenic processes. This method does not eliminate natural variability, but instead provides a clearer view of self-organized depositional behavior. As a result, the findings represent a purely autogenic process. In nature, the combination of autogenic reorganization and different allogenic forcing interactions would produce more complex and layered stacking patterns over time.

The experimental results of this study demonstrate that autogenic processes generate complex stacking patterns in submarine lobe systems. Each experiment developed a unique lobate deposit with different stacking patterns (aggradation, retrogradation, and compensation) (Figures 3C, 4C, 6C, 7). These stacking pattern evolutions can be used to interpret the stacking patterns observed in outcrops of the submarine lobe system.

The thickening and thinning upward trends in the submarine fan lobe systems suggest variations in depositional environments and factors. A thickening upward trend in the lobe is commonly interpreted as resulting from a continuous sediment supply from continental environments with high flow energy, combined with a subsequent drop in sea level. This results in a progradational pattern (Catuneanu, 2006; Grundvåg et al., 2014; Hodgson et al., 2016). In contrast, a thinning upward trend in the lobe is generally interpreted as a relative sea level rise, resulting from reduced sediment supply or flow energy, which leads to a retrogradational and backstepping stacking pattern (e.g., Catuneanu, 2006). These trends are attributed to allogenic controls (Normark et al., 2006; Knudson and Hendy, 2009). However, this interpretation may not always be accurate, as internal dynamic systems (autogenic processes) also influence the stacking patterns of submarine fan lobes. The experimental basin floor deposits developed in this study provide a clear demonstration of this effect.

5 Conclusion

This study documented the stacking patterns, flow field evolution and sediment distribution in submarine fan systems driven by autogenic factors. Three series of experiments were conducted under constant boundary conditions at the Eurotank laboratory to determine the impact of autogenic factors on submarine lobe development.

The major outcomes are:

1. We observed aggradational, compensational, and retrogradational stacking patterns in Series 2 and 3. However, except for the initial establishment of basin floor deposition during the first run of the series, no progradational stacking patterns were observed. This suggests that autogenic processes alone are not sufficient to create progradational stacking patterns and that additional allogenic influences could play a role.
2. Morphodynamic feedback from subsequent flows showed a reduction in flow velocity and an increase in lateral spreading of deposits in successive runs leading to retrogradational stacking patterns and the creation of channel wings.
3. Sediment distribution between channel and basin floor deposits was governed not only by morphodynamic feedback, but also by channel geometry, sediment concentration, and heavy mineral content. Narrow, confined channels favored sediment delivery to the basin floor, whereas wide, shallow channels resulted in significant sedimentation in the channel.
4. These results have significant stratigraphic implications for the interpretation of compensational, aggradational, and retrogradational stacking patterns, as well as upward-thinning trends that develop through autogenic processes. Therefore, analysis of these patterns in the geological record should consider potential autogenic causes rather than attributing them exclusively to decreased sediment supply or relative sea-level rise.

Future research will prioritize the integration of changing allogenic boundary conditions to clarify how autogenic and allogenic factors jointly govern the development of submarine lobes.

Data availability statement

The raw data supporting the conclusions of this article will be made available by the authors, without undue reservation.

Author contributions

LZ: Writing – original draft, Project administration, Formal Analysis, Data curation, Writing – review and editing, Visualization, Conceptualization, Investigation, Methodology, Validation. AP: Data curation, Investigation, Formal Analysis, Writing – original draft, Writing – review and editing, Visualization. PA: Writing – review and editing, Resources, Methodology. JE: Formal Analysis, Methodology, Resources, Project administration, Supervision, Conceptualization, Writing – review and editing. JW: Project administration, Supervision, Writing – review and editing, Funding acquisition. YS: Formal Analysis, Writing – review and editing, Project administration, Supervision, Writing – original draft, Methodology, Validation, Investigation, Resources, Conceptualization, Funding acquisition.

Funding

The author(s) declared that financial support was received for this work and/or its publication. This work was financed by a research grant of the Deutsche Forschungsgemeinschaft (DFG; project number: 525486108) as part of the project: "Allogenic vs. Autogenic processes: On the preservation and shredding of environmental signals in submarine fans (AvaFan)".

Acknowledgements

It is a pleasure to thank the DFG for its funding and Utrecht University for hosting us during the experiments. We are grateful to the Editor Dicky Harishidayat for handling the manuscript, and the three reviewers for their constructive feedback, which helped improve this manuscript.

Conflict of interest

The author(s) declared that this work was conducted in the absence of any commercial or financial relationships that could be construed as a potential conflict of interest.

Generative AI statement

The author(s) declared that generative AI was not used in the creation of this manuscript.

Any alternative text (alt text) provided alongside figures in this article has been generated by Frontiers with the support of artificial intelligence and reasonable efforts have been made to ensure accuracy, including review by the authors wherever possible. If you identify any issues, please contact us.

Publisher's note

All claims expressed in this article are solely those of the authors and do not necessarily represent those of their affiliated organizations, or those of the publisher, the editors and the reviewers. Any product that may be evaluated in this article, or claim that may be made by its manufacturer, is not guaranteed or endorsed by the publisher.

Supplementary material

The Supplementary Material for this article can be found online at: https://www.frontiersin.org/articles/10.3389/feart.2026.1759842/full#supplementary-material

SUPPLEMENTARY FIGURE S1
The Shields mobility diagram offers an overview of the experimental conditions.

References

Alves, E., and Rossatto, R. (2011). "Experimental study of turbidity currents flow around obstacles," in *7th International Symposium on Stratified Flows (ISSF) (Rome)*.

Alves, E., González, J., Freire, P., and Cardoso, A. (2008). *Experimental study of plunging turbidity currents in reservoirs*.

Baas, J. H., McCaffrey, W. D., Haughton, P. D. W., and Choux, C. (2005). Coupling between suspended sediment distribution and turbulence structure in a laboratory turbidity current. *J. Geophys. Res. Oceans* 110 (C11), 2004JC002668. doi:10.1029/2004JC002668

Beerbower, J. R. (1964). Cyclothems and cyclic depositional mechanisms in alluvial plain sedimentation. *Kans. Geol. Surv. Bull.* 169, 31–32.

Bell, D., Soutter, E. L., Cumberpatch, Z. A., Ferguson, R. A., Spychala, Y. T., Kane, I. A., et al. (2021). Flow-process controls on grain type distribution in an experimental turbidity current deposit: implications for detrital signal preservation and microplastic distribution in submarine fans. *Depositional Rec.* 7, 392–415. doi:10.1002/dep2.153

Blum, M., Rogers, K., Gleason, J., Najman, Y., Cruz, J., and Fox, L. (2018). Allogenic and autogenic signals in the stratigraphic record of the deep-sea bengal fan. *Sci. Rep.* 8, 7973. doi:10.1038/s41598-018-25819-5

Burgess, P. M., Masiero, I., Toby, S. C., and Duller, R. A. (2019). A big fan of signals? Exploring autogenic and allogenic process and product in a numerical stratigraphic forward model of submarine-fan development. *J. Sediment. Res.* 89 (1), 1–12. doi:10.2110/jsr.2019.3

Burgess, P. M., and Duller, R. A. (2024). Autogenic masking of allogenic inputs: numerical modelling of signal preservation in deep-water fan strata. *Earth Planet. Sci. Lett.* 628, 118583. doi:10.1016/j.epsl.2024.118583

Cartigny, M. J. B., Eggenhuisen, J. T., Hansen, E. W. M., and Postma, G. (2014). Concentration-Dependent flow stratification in experimental high-density turbidity currents and their relevance to turbidite facies models. *J. Sediment. Res.* 83, 1046–1064. doi:10.2110/jsr.2013.71

Carvajal, C., and Steel, R. (2011). Source-to-sink sediment volumes within a tectono-stratigraphic model for a laramide shelf-to-deep-water basin: methods and results. *Tecton. Sediment. Basins Recent Adv.*, 131–151. doi:10.1002/9781444347166.ch7

Casagrande, J., Hodgson, D. M., and Peakall, J. (2024). A salty snapshot: extreme variations in basal erosion patterns preserved in a submarine channel. *J. Geol. Soc.* 181, jgs2023-006. doi:10.1144/jgs2023-006

Catuneanu, O. (2006). *Principles of sequence stratigraphy*. Amsterdam Paris: Elsevier.

Catuneanu, O., Khalifa, M. A., and Wanas, H. A. (2006). Sequence stratigraphy of the lower cenomanian bahariya formation, bahariya oasis, Western desert, Egypt. *Sediment. Geol.* 190, 121–137. doi:10.1016/j.sedgeo.2006.05.010

Cornard, P. H., and Kevin, T. P. (2020). Submarine topographic control on distribution of supercritical-flow deposits in lobe and related environments, Middle Eocene, Jaca Basin, Spanish Pyrenees. *J. Sediment. Res.* 90 (9), 1222–1243. doi:10.2110/jsr.2020.59

Covault, J. A., Normark, W. R., Romans, B. W., and Graham, S. A. (2007). Highstand fans in the California Borderland: the overlooked deep-water depositional systems. *Geology* 35 (9), 783. doi:10.1130/G23800A.1

Covault, J. A., Fildani, A., Romans, B. W., and McHargue, T. (2011). The natural range of submarine canyon-and-channel longitudinal profiles. *Geosphere* 7 (2), 313–332. doi:10.1130/GES00610.1

De Leeuw, J., Eggenhuisen, J. T., and Cartigny, M. J. B. (2016). Morphodynamics of submarine channel inception revealed by new experimental approach. *Nat. Commun.* 7, 10886. doi:10.1038/ncomms10886

De Leeuw, J., Eggenhuisen, J. T., Spychala, Y. T., Heijnen, M. S., Pohl, F., and Cartigny, M. J. B. (2018). Sediment volume and grain-size partitioning between submarine channel–levee systems and lobes: an experimental study. *J. Sediment. Res.* 88, 777–794. doi:10.2110/jsr.2018.46

Deptuck, M. E., and Sylvester, Z. (2018). "Submarine fans and their channels, levees, and lobes," in *Submarine geomorphology, springer geology*. Editors A. Micallef, S. Krastel, and A. Savini (Cham: Springer International Publishing), 273–299. doi:10.1007/978-3-319-57852-1_15

Deptuck, M. E., Sylvester, Z., Pirmez, C., and O'Byrne, C. (2007). Migration–aggradation history and 3-D seismic geomorphology of submarine channels in the Pleistocene Benin-major Canyon, western Niger Delta slope. *Mar. Pet. Geol.* 24, 406–433. doi:10.1016/j.marpetgeo.2007.01.005

Deptuck, M. E., Piper, D. J. W., Savoye, B., and Gervais, A. (2008). Dimensions and architecture of late Pleistocene submarine lobes off the northern margin of East Corsica. *Sedimentology* 55, 869–898. doi:10.1111/j.1365-3091.2007.00926.x

Elliott, T. (2000). *Megaflute erosion surfaces and the initiation of turbidite channels*.

Ferguson, R. A., Kane, I. A., Eggenhuisen, J. T., Pohl, F., Tilston, M., Spychala, Y. T., et al. (2020). Entangled external and internal controls on submarine fan evolution: an experimental perspective. *Depositional Rec.* 6, 605–624. doi:10.1002/dep2.109

Fernandes, A. M., Buttles, J., and Mohrig, D. (2020). Flow substrate interactions in aggrading and degrading submarine channels. *J. Sediment. Res.* 90, 573–583. doi:10.2110/jsr.2020.31

Fick, C., Manica, R., and Toldo Junior, E. E. (2017). Autogenic influence on the morphology of submarine fans: an approach from 3D physical modelling of turbidity currents. *Braz. J. Geol.* 47, 345–368. doi:10.1590/2317-4889201720170066

Garcia, M. (2008). *Sedimentation engineering: processes, measurements, modeling, and practice*. Reston, VA: ASCE Manuals and Reports on Engineering Practice No. 110, American Society of Civil Engineers.

Grime, R., Sorrel, P., Boulesteix, K., Landru, S., Bouche, A., Rice, T., et al. (2024). Autogenic and allogenic controls on turbidite lobe stacking pattern and architecture: the case of the Turonian to Coniacian deep-water turbidite lobe complexes (Dønna Terrace, offshore Mid-NORWAY). *Sedimentology* 71, 419–456. doi:10.1111/sed.13141

Grundvåg, S., Johannessen, E. P., Helland-Hansen, W., and Plink-Björklund, P. (2014). Depositional architecture and evolution of progradationally stacked lobe complexes in the Eocene Central Basin of Spitsbergen. *Sedimentology* 61, 535–569. doi:10.1111/sed.12067

Hamilton, P. B., Strom, K. B., and Hoyal, D. C. J. D. (2015). Hydraulic and sediment transport properties of autogenic avulsion cycles on submarine fans with supercritical distributaries. *J. Geophys. Res. Earth Surf.* 120, 1369–1389. doi:10.1002/2014JF003414

Hay, A. E., and Speller, R. (2005). Naturally occurring scour pits in nearshore sands. *J. Geophys. Res. Earth Surf.* 110. doi:10.1029/2004jf000199

Hiscott, R. N. (1994). Loss of capacity, not competence, as the fundamental process governing deposition from turbidity currents. *J. Sediment. Res.* 64, 209–214. doi:10.2110/jsr.64.209

Hitomi, J., Nomura, S., Murai, Y., De Cesare, G., Tasaka, Y., Takeda, Y., et al. (2021). Measurement of the inner structure of turbidity currents by ultrasound velocity profiling. *Int. J. Multiph. Flow* 136, 103540. doi:10.1016/j.ijmultiphaseflow.2020.103540

Hodgson, D. M., Kane, I. A., Flint, S. S., Brunt, R. L., and Ortiz-Karpf, A. (2016). Time-Transgressive confinement on the slope and the progradation of basin-floor fans: implications for the sequence stratigraphy of deep-water deposits. *J. Sediment. Res.* 86, 73–86. doi:10.2110/jsr.2016.3

Hubbard, S. M., De Ruig, M. J., and Graham, S. A. (2009). Confined channel-levee complex development in an elongate depo-center: deep-water tertiary strata of the Austrian Molasse basin. *Mar. Pet. Geol.* 26, 85–112. doi:10.1016/j.marpetgeo.2007.11.006

Hubbard, S. M., Covault, J. A., Fildani, A., and Romans, B. W. (2014). Sediment transfer and deposition in slope channels: deciphering the record of enigmatic deep-sea processes from outcrop. *Geol. Soc. Am. Bull.* 126 (5–6), 857–871. doi:10.1130/B30996.1

Jegou, I., Savoye, B., Pirmez, C., and Droz, L. (2008). Channel-mouth lobe complex of the recent Amazon Fan: the missing piece. *Mar. Geol.* 252, 62–77. doi:10.1016/j.margeo.2008.03.004

Jerolmack, D. J., and Paola, C. (2010). Shredding of environmental signals by sediment transport. *Geophys. Res. Lett.* 37, 2010GL044638. doi:10.1029/2010GL044638

Kneller, B., and Buckee, C. (2000). The structure and fluid mechanics of turbidity currents: a review of some recent studies and their geological implications. *Sedimentology* 47 (s1), 62–94. doi:10.1046/j.1365-3091.2000.047s1062.x

Knudson, K. P., and Hendy, I. L. (2009). Climatic influences on sediment deposition and turbidite frequency in the Nitinat Fan, British Columbia. *Mar. Geol.* 262, 29–38. doi:10.1016/j.margeo.2009.03.002

Konsoer, K., Zinger, J., and Parker, G. (2013). Bankfull hydraulic geometry of submarine channels created by turbidity currents: relations between bankfull channel characteristics and formative flow discharge. *J. Geophys. Res. Earth Surf.* 118 (1), 216–228. doi:10.1029/2012JF002422

Kuenen, P. H., and Migliorini, C. (1950). Turbidity currents as a cause of graded bedding. *J. Geol.* 58, 91–127. doi:10.1086/625710

Lamb, M. P., Parsons, J. D., Mullenbach, B. L., Finlayson, D. P., Orange, D. L., and Nittrouer, C. A. (2008). Evidence for superelevation, channel incision, and formation of cyclic steps by turbidity currents in eel canyon, California. *Geol. Soc. Am. Bull.* 120 (3–4), 463–475. doi:10.1130/B26184.1

Li, S., Ding, S., Wu, D., Wang, X., Hao, Y., Li, Q., et al. (2021). Analysis of stratum subsidence induced by depressurization at an offshore hydrate-bearing sediment. *Energy & Fuels* 35 (2), 1381–1388. doi:10.1021/acs.energyfuels.0c03833

Meiburg, E., and Kneller, B. (2010). Turbidity currents and their deposits. *Annu. Rev. Fluid Mech.* 42 (1), 135–156. doi:10.1146/annurev-fluid-121108-145618

Middleton, G. V. (1993). Sediment deposition from turbidity currents. *Annu. Rev. Earth Planet. Sci.* 21 (89), 89–114. doi:10.1146/annurev.earth.21.1.89

Middleton, G. V., and Hampton, M. A. (1973). Part I. Sediment gravity flows: mechanics of flow and deposition.

Middleton, G., and Southard, J. B. (1984). *Behavior of fluids*.

Morris, P. D., Sylvester, Z., Covault, J. A., Mohrig, D., and Dunlap, D. (2024). Fluvial-style migration controls autogenic aggradation in submarine channels: Joshua Channel, eastern Gulf of Mexico. *Geol. Soc. Lond. Spec. Publ.* 540, 265–280. doi:10.1144/sp540-2022-123

Normark, W. R., Piper, D. J. W., and Sliter, R. (2006). Sea-level and tectonic control of middle to late pleistocene turbidite systems in Santa Monica Basin, offshore California. *Sedimentology* 53, 867–897. doi:10.1111/j.1365-3091.2006.00797.x

Parker, G., Fukushima, Y., and Pantin, H. M. (1986). Self-accelerating turbidity currents. *J. Fluid Mech.* 171, 145–181. doi:10.1017/S0022112086001404

Paull, C. K., Talling, P. J., Maier, K. L., Parsons, D., Xu, J., Caress, D. W., et al. (2018). Powerful turbidity currents driven by dense basal layers. *Nat. Commun.* 9 (1), 4114. doi:10.1038/s41467-018-06254-6

Payros, A., and Pujalte, V. (2008). Calciclastic submarine fans: an integrated overview. *Earth-Science Rev.* 86 (1–4), 203–246. doi:10.1016/j.earscirev.2007.09.001

Peakall, J., and Sumner, E. J. (2015). Submarine channel flow processes and deposits: a process-product perspective. *Geomorphology* 244, 95–120. doi:10.1016/j.geomorph.2015.03.005

Picot, M., Droz, L., Marsset, T., Dennielou, B., and Bez, M. (2016). Controls on turbidite sedimentation: insights from a quantitative approach of submarine channel and lobe architecture (Late Quaternary Congo Fan). *Mar. Pet. Geol.* 72, 423–446. doi:10.1016/j.marpetgeo.2016.02.004

Piper, D. J. W., and Normark, W. R. (1983). Turbidite depositional patterns and flow characteristics, Navy Submarine Fan, California borderland. *Sedimentology* 30 (5), 681–694. doi:10.1111/j.1365-3091.1983.tb00702.x

Pirmez, C., and Imran, J. (2003). Reconstruction of turbidity currents in Amazon Channel. *Mar. Pet. Geol.* 20, 823–849. doi:10.1016/j.marpetgeo.2003.03.005

Pohl, F., Eggenhuisen, J. T., Cartigny, M. J. B., Tilston, M. C., De Leeuw, J., and Hermidas, N. (2020). The influence of a slope break on turbidite deposits: an experimental investigation. *Mar. Geol.* 424, 106160. doi:10.1016/j.margeo.2020.106160

Posamentier, H. W., and Kolla, V. (2003). Seismic geomorphology and stratigraphy of depositional elements in deep-water settings. *J. Sediment. Res.* 73, 367–388. doi:10.1306/111302730367

Postma, G., and Kick, K. (2018). Supercritical flows and their control on the architecture and facies of small-radius sand-rich fan lobes. *Sediment. Geol.* 364, 53–70. doi:10.1016/j.sedgeo.2017.11.015

Prather, B. E., O'Byrne, C., Pirmez, C., and Sylvester, Z. (2017). Sediment partitioning, continental slopes and base-of-slope systems. *Basin Res.* 29, 394–416. doi:10.1111/bre.12190

Prélat, A., and Hodgson, D. M. (2013). The full range of turbidite bed thickness patterns in submarine lobes: controls and implications. *J. Geol. Soc.* 170, 209–214. doi:10.1144/jgs2012-056

Prélat, A., Hodgson, D. M., and Flint, S. S. (2009). Evolution, architecture and hierarchy of distributary deep-water deposits: a high-resolution outcrop investigation from the Permian Karoo Basin, South Africa. *Sedimentology* 56, 2132–2154. doi:10.1111/j.1365-3091.2009.01073.x

Pyrcz, M. J., Catuneanu, O., and Deutsch, C. V. (2005). Stochastic surface-based modeling of turbidite lobes. *AAPG Bull.* 89 (2), 177–191. doi:10.1306/09220403112

Romans, B. W., Castelltort, S., Covault, J. A., Fildani, A., and Walsh, J. P. (2016). Environmental signal propagation in sedimentary systems across timescales. *Earth-Sci. Rev.* 153, 7–29. doi:10.1016/j.earscirev.2015.07.012

Sahoo, H., Gani, M. R., Gani, N. D., Hampson, G. J., Howell, J. A., Storms, J. E. A., et al. (2020). Predictable patterns in stacking and distribution of channelized fluvial sand bodies linked to channel mobility and avulsion processes. *Geology* 48, 903–907. doi:10.1130/G47236.1

Scacchia, E., Tinterri, R., and Gamberi, F. (2024). Downslope evolution of supercritical bedforms in a confined deep-sea fan lobe, Amantea fan, Paola Basin (Southeastern Tyrrhenian Sea). *Sediment. Geol.* 466, 106636. doi:10.1016/j.sedgeo.2024.106636

Shields, A. (1936). Application of similarity mechanics and turbulence research to sediment transport. Berlin: Prussian Research Institute for Hydraulic Engineering and Shipbuilding.

Soutter, E. L., Bell, D., Cumberpatch, Z. A., Ferguson, R. A., Spychala, Y. T., Kane, I. A., et al. (2021). The influence of confining topography orientation on experimental turbidity currents and geological implications. *Front. Earth Sci.* 8, 540633. doi:10.3389/feart.2020.540633

Spychala, Y. T., Eggenhuisen, J. T., Tilston, M., and Pohl, F. (2020). The influence of basin setting and turbidity current properties on the dimensions of submarine lobe elements. *Sedimentology* 67, 3471–3491. doi:10.1111/sed.12751

Spychala, Y., Burgess, P., and Stevenson, C. (2024). (Dis) Order in submarine fans at different observational scales: an example from Unit A of the Laingsburg formation, Karoo Basin. *The Sedimentary Record* 22 (1). doi:10.2110/001c.125001

Straub, K. M., and Mohrig, D. (2009). Constructional canyons built by sheet-like turbidity currents: observations from offshore Brunei Darussalam. *J. Sediment. Res.* 79 (1), 24–39. doi:10.2110/jsr.2009.006

Straub, K. M., and Pyles, D. R. (2012). Quantifying the hierarchical organization of compensation in submarine fans using surface statistics. *J. Sediment. Res.* 82 (11), 889–898. doi:10.2110/jsr.2012.73

Straub, K. M., Paola, C., Mohrig, D., Wolinsky, M. A., and George, T. (2009). Compensational stacking of channelized sedimentary deposits. *J. Sediment. Res.* 79, 673–688. doi:10.2110/jsr.2009.070

Straub, K. M., Mohrig, D., and Pirmez, C. (2012). *Architecture of an aggradational tributary submarine-channel network on the continental slope offshore Brunei Darussalam*.

Sylvester, Z., Deptuck, M. E., Prather, B. E., Pirmez, C., and O'byrne, C. (2012). Seismic stratigraphy of a shelf-edge delta and linked submarine channels in the northeastern Gulf of Mexico. doi:10.2110/pec.12.99.0031

Talling, P. J., Masson, D. G., Sumner, E. J., and Malgesini, G. (2012). Subaqueous sediment density flows: depositional processes and deposit types. *Sedimentology* 59, 1937–2003. doi:10.1111/j.1365-3091.2012.01353.x

Van Der Merwe, W. C., Hodgson, D. M., Brunt, R. L., and Flint, S. S. (2014). Depositional architecture of sand-attached and sand-detached channel-lobe transition zones on an exhumed stepped slope mapped over a 2500 km^2 area. *Geosphere* 10, 1076–1093. doi:10.1130/ges01035.1

Van Rijn, L. C., Nieuwjaar, M. W. C., Van Der Kaay, T., Nap, E., and Van Kampen, A. (1993). Transport of fine sands by currents and waves. *J. Waterw. Port. Coast. Ocean. Eng.* 119, 123–143. doi:10.1061/(ASCE)0733-950X(1993)119:2(123)

Wang, L.-P., and Maxey, M. R. (1993). Settling velocity and concentration distribution of heavy particles in homogeneous isotropic turbulence. *J. Fluid Mech.* 256, 27–68. doi:10.1017/S0022112093002708

Wynn, R. B., Piper, D. J. W., and Gee, M. J. R. (2002). Generation and migration of coarse-grained sediment waves in turbidity current channels and channel–lobe transition zones. *Mar. Geol.* 192 (1–3), 59–78. doi:10.1016/S0025-3227(02)00549-2